# Circuit Configuration and Control of a Grid-Tie Small-Scale Wind Generation System for Expanded Wind Speed Range

Chengshan Wang, *Senior Member, IEEE*, Liang Yang, Yifeng Wang, *Member, IEEE*, Zhun Meng, Wei Li, and Fuqiang Han

***Abstract*—In this paper, a grid-tie small-scale wind generation system is proposed with innovations in both of the topology and the controller. A novel high step-up zero-current turning-on soft-switching rectifier and a storage branch are employed to improve the low-wind-speed (LWS) and high-wind-speed (HWS) performances. The optimized LWS operation is guaranteed by the rectifier, the battery pack, and film capacitors. The enhanced HWS performance is fulfilled by parallel operation of the inverter and the battery charge converter. Furthermore, the control strategy aiming at improving overall system efficiency and extending battery lifespan and exploitable wind speed range is adopted. A state-of-charge (SOC) control method is used and ensures SOC is most frequently within a range of 20–80%. The proposed method not only slows down the battery capacity fading by SOC scope limitation and by charge/discharge current restriction, but also provides safety capacity margin in case of extreme HWS condition. Also, a simple but reliable dead-zone controller is applied on the battery charge/discharge converter to control the dc-link voltage. Finally, the theoretical analysis and the control method are verified by simulations, experiments, and are tested in the real wind field.**

***Index Terms*—Expanded wind speed range, grid-tie wind power generation, high voltage gain, small-scale wind generation system, state-of-charge (SOC).**

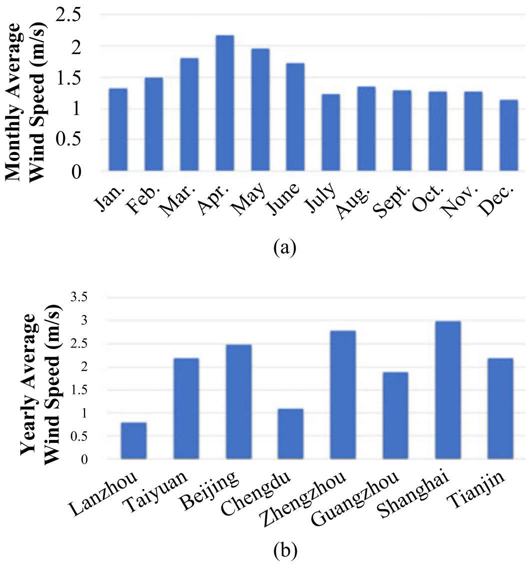

(a)

(b)

Fig. 1. Historical statistical wind speed data (a) measured by an anemograph and (b) recorded by the National Meteorological Administration.

## I. INTRODUCTION

EXCESSIVE consumption of exhaustible fossil fuels has resulted in grave outcomes such as the energy crisis and the severely contaminated environment. Fortunately, renewable energies, as promising solutions to alleviate these problems, have attracted significant attentions. As one of the most competitive alternatives, wind power generation has become a hotspot. Distinguished by power grades, the medium- to large-scale wind applications can provide adequate power with less fluctuation, and hence, their relatively stable power supply renders the medium- to large-scale WGS suitable for extensive commercial applications [1]–[3]. Plenty of relevant studies are conducted and mature technologies have been achieved. However, imperfections such as difficulties in transportation, installation, maintenance, and large impacts on the main grid still exist. Free from these problems, the SWGS becomes another effective attempt for wind application. Owing to low cost, high flexibility, and adjustable installation capacity, the SWGS can act as an auxiliary power source for house lighting, mobile phone charge, etc. It is generally positioned in spare space such as building roofs, remote areas like islands, mountainous regions, and grasslands [4]–[7]. Unfortunately, its extensive usage is hampered by the insufficient and erratic power supply in the wind field.

Fig. 1 shows the historical statistical wind speed data measured by an anemograph and recorded by the National Meteorological Administration, respectively [8]. Fig. 1(a) shows the monthly average wind speed data of the year 2015, which were measured at a certain building roof in Tianjin, China. It illustrates that the average speed is always below the cut-in wind speed (normally around $3\,\mathrm{m/s}$) of most current wind turbines.

Manuscript received January 27, 2016; revised June 1, 2016 and July 29, 2016; accepted September 5, 2016. Date of publication September 13, 2016; date of current version February 27, 2017. This work was supported in part by National High Technology Research and Development Program 863 of China (2015AA050603), in part by the National Natural Science Foundation of China (Grant 51307117), and in part by the Key project of Tianjin Science and Technology Support Program, China (14ZCZDGX00035). Recommended for publication by Associate Editor M. Molinas.

The authors are with the Key Laboratory of Smart Grid of Ministry of Education, Tianjin University, Tianjin 300072, China (e-mail: cswang@tju.edu.cn; zyangliang@tju.edu.cn; wayif@tju.edu.cn; quakermaster@hotmail.com; liweitju@hotmail.com; hanxingyu@tju.edu.cn).

Color versions of one or more of the figures in this paper are available online at http://ieeexplore.ieee.org.

Digital Object Identifier 10.1109/TPEL.2016.2608909

Thus, it only sustains a sparse power output or even no output in most grid-tie small-scale wind generation system (GT-SWGS). This statistical finding is universally applicable for all small-scale wind fields (SWFs) according to Fig. 1(b). This figure shows the yearly average wind speed of several cities, and the outcomes are consistent with those of Fig. 1(a). Besides, being sensitive to terrain topography, intensive fluctuations also exist in SWFs and increase difficulty in SWGS design.

To develop solutions to these shortcomings, several studies on the SWGS have been done as depicted in [4]–[7] and [9]–[23]. These systems can be divided into two main types: the stand-alone and the grid-tie system. The stand-alone SWGS (SA-SWGS), [4]–[6] and [9]–[15], in which wind power is directly transferred to the off-grid load, generally draws more attention owing to its simple structure and low cost. With respect to topology, almost every stand-alone system employs the classic configuration consisting of a three-phase diode bridge, a buck circuit, and a dc load. This simple configuration possesses high reliability and ease of control. Then based on this structure, several advanced control strategies have been proposed, most of which are intended to develop maximum power point tracking (MPPT) algorithms with fast speed and enhanced accuracy [10]–[13], [24]–[27]. Through these MPPT methods, the stand-alone systems harvest outstanding maximum power extraction and dynamic response, and therefore, show high adaptability to the SWF. Nevertheless, despite these advantages, extensive application of the SA-SWGS is challenged by limitations of the load, because the available load range is narrow and needs to be specially selected. Another drawback is that the unexpected storage losses and battery discharge losses are inevitably introduced as many SA-SWGS employ a battery with large capacity to store wind power for further usage. These losses may even counteract the extra energy saved by MPPT methods.

The GT-SWGS, as the other main type for small-scale wind applications, is able to convert the captured wind power into the unified ac grid power, and thus it has an expanded application range. Based on two main types of system configurations, GT-SWGS have been implemented in [7] and [16]–[23]. The authors of [16]–[19] have proposed several control schemes based on the commonly used back-to-back pulse width modulation (PWM) converters. In [16], a comprehensive control strategy including adaptive search control, fuzzy logic control, and vector control technique is proposed. This system is outstanding owing to its high efficiency and extension of the exploitable wind speed range. Nevertheless, this system is designed based on the squirrel cage induction generator and requires an extra expensive gear box, which needs regular maintenance and may reduce the system reliability. While in [17], based on the more cost-effective permanent magnet synchronous generator (PMSG), the authors believe that an optimum small-scale system should not focus only on the tracking speed and accuracy of the MPPT algorithm, but also need to consider the dynamic load which has an impact on the lifespan of the SWGS. This dynamic load is classified and its interrelation with the tracking speed is shown. In the end, a novel control method to attenuate the dynamic load is presented and is experimentally verified to function well. However, this literature does not discuss the control for low power condition, and thus it cannot prove an outstanding low-wind-speed (LWS) performance, which is significant to the GT-SWGS. From different perspective, another system configuration is studied in [7] and [20]–[23]. This cost-effective alternative is composed of a three-phase diode bridge, a boost chopper, and an inverter. Indeed, this structure is often preferred because the cost is one of the primary issues in the SWGS. In [21], similar functions as MPPT and enhanced dynamic behavior are also realized. Besides, a dummy load is adopted to consume the surplus power beyond the rated wind speed, which extends the exploitable range at high-wind-speed (HWS). However, it also neglects to analyze the important LWS performance.

According to the aforesaid analysis, most existing GT-SWGS only focus on the advanced control methods as MPPT, dynamic response, and HWS protection. Few of them have researched from the system topology perspective, i.e., most GT-SWGS do not employ a battery, which is proved to be indispensable in this paper. Besides, these methods are often verified in the laboratory with ideal power supply (usually $> 1$ kW). Few of them have investigated on the characteristics of the SWF and has given practical grid-tie generation results in the real wind field. Considering the limitations inferred from Fig. 1, there are still many problems to be improved in the existing GT-SWGS especially at LWS.

1) Limited voltage gain. Owing to the frequent LWS, the system has to be operated with insufficient power. Actually, this power has always been wasted that with limited voltage gain, both of the back-to-back and the cost-effective systems fail to reach the minimum requirement of dc-link voltage for grid-connection. The GT-SWGS cannot conduct grid-tie generation normally.

Several potential technologies are considered for voltage improvement. In [28]–[30], flyback converters suitable for high frequency, low power, and high voltage gain applications are proposed, while literatures [31]–[33] use switched capacitors to pursue high-voltage conversion. However, although both of them function well in dc–dc applications, they cannot be transplanted into ac–dc converters directly. Thus, an additional front-stage rectifier is needed, which may lead to efficiency fading, higher cost, and more complicated control. To avoid this, novel high step-up single-stage ac–dc converter is needed.

2) Lack of storage component. In existing GT-SWGS, the frequent low input power usually fails to drive the grid-tie generation even with advanced MPPT methods. This power often dissipates in the dc-link electrolytic capacitor as heat and leads to low wind power utilization rate. In addition, the fluctuations in wind speed also make the grid-tie generation unstable. The storage component can solve all these problems. It helps to establish the grid-connection and smooths fluctuations, thereby becomes an indispensable part in the GT-SWGS.
3) Restricted available wind speed range. Besides the limited LWS range, many systems do not consider about the HWS performance either.

In this paper, a PMSG-based GT-SWGS is presented. To enhance the adaptability to the SWF, improvements in both of the topology and the controller are made. In Section II, a three-phase single-stage high step-up zero-current turning-on (ZCT-ON) rectifier are proposed. Besides, a battery pack is also

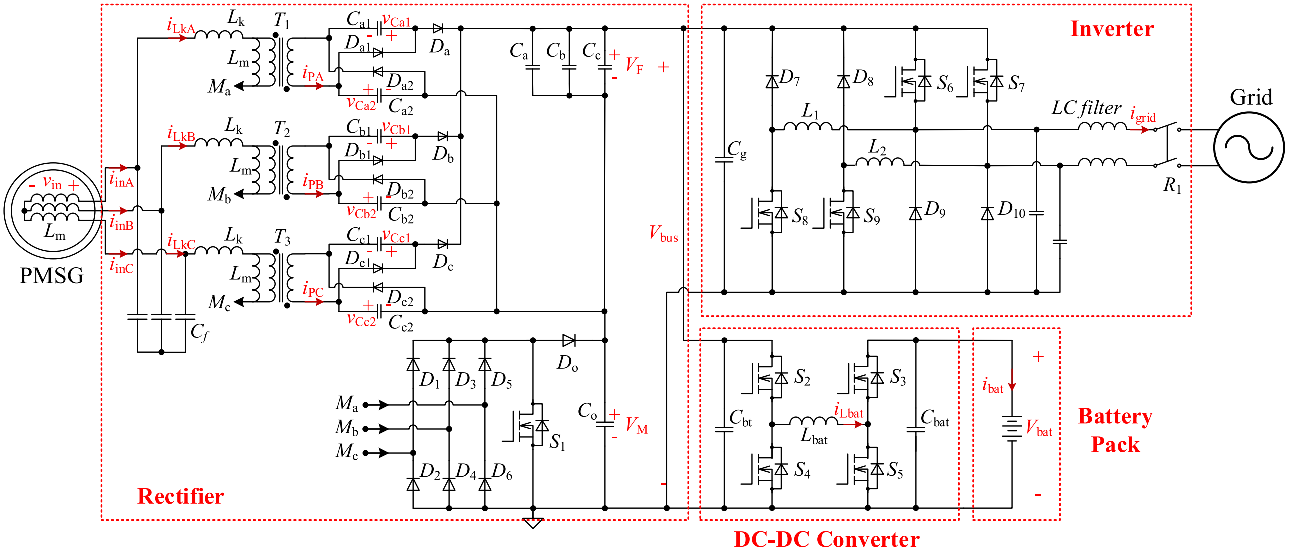

Fig. 2. Topology of the proposed GT-SWGS.

introduced into the system. It acts as an auxiliary source to facilitate the efficient grid-tie generation, and as a storage to absorb weak wind power and to broaden exploitable HWS range. In Sections III and IV, the system control strategy and the dc-link voltage control are discussed, respectively. The controller adopts relevant methods for different wind speeds, and the battery lifespan is also considered. In Section V, to verify the feasibility and practicability, the proposed GT-SWGS is tested in both of the laboratory and the real SWF. Finally, the conclusion is drawn in Section VI.

## II. PROPOSED SYSTEM

The topology of the proposed GT-SWGS is presented in Fig. 2. Four main parts constitute the entire system, including the novel rectifier, a single-phase dual-buck inverter, a bidirectional dc–dc converter and a battery pack. For system topology, two main points are distinguished from others: the introduction of the dc–dc converter and battery pack into the GT-SWGS and the adoption of the three-phase high step-up ZCT-ON rectifier. By integrating flyback structure, switched capacitors and three-phase single-switch boost (TSB) circuit [28], [34], this novel rectifier can provide high voltage gain with wide variable range and ZCT-ON. At LWS, the rectifier, the storage branch and film capacitors assist to collect weak wind power under stand-alone mode. At HWS, the battery pack absorbs surplus input power to broaden the exploitable power range. This study also talks about the selection criteria of the battery pack briefly and points out the reasonable usage method to prolong battery lifespan.

### *A. High Step-Up Discontinuous Current Mode (DCM) Rectifier*

In Fig. 2, the proposed rectifier is shown, which is composed of three main parts: filter capacitors $C_f$, three flyback cells, and a TSB cell ($L_k$, $D_1 - D_6$, $S_1$, $D_o$, and $C_o$). Taking phase A, for example, the flyback cell is made up of the flyback transformer $T_1$, a pair of switched capacitor cells ($C_{a1}$, $D_{a1}$ and $C_{a2}$, $D_{a2}$), the freewheeling diode $D_a$, and the output capacitor $C_a$. When the switched capacitor cells. $C_{a1}$ and $C_{a2}$ store this power and transfer it to $C_a$ through $D_a$ eventually. Meanwhile, the remaining ac power is converted and sent to $C_o$. Finally, the flyback output voltage $V_F$ is superimposed on the TSB output voltage $V_M$, and the dc-link voltage $V_{\text{bus}}$ is promoted. Besides, the equivalent wind turbine inductor $L_m$, the transformer leakage inductor $L_k$ and $C_f$ form a *LCL* filter, and the high-frequency components in currents $i_{\text{LkA}}$, $i_{\text{LkB}}$, and $i_{\text{LkC}}$ of $L_k$ are filtered by $C_f$, which will attenuate the vibration and noise of the turbine.

The characteristics of the proposed rectifier are listed as follows:

1) High voltage gain: The rectifier voltage gain is defined as $M_{\text{gain}} = V_{\text{bus}} / v_{\text{in-RMS}}$, where $v_{\text{in-RMS}}$ represents the RMS value of input phase voltage $v_{\text{in}}$ (including $v_{\text{in}A}$, $v_{\text{in}B}$ and $v_{\text{in}C}$). With insufficient wind power, the rectifier can offer high $M_{\text{gain}}$ and boost $V_{\text{bus}}$ to suit for the battery voltage $V_{\text{bat}}$ so that the weak input power is collected with improved efficiency; high $M_{\text{gain}}$ also helps the inverter to conduct grid-tie generation at lower input voltage.
2) Widely variable voltage gain range: $M_{\text{gain}}$ varies within a wide range and has a nearly linear relationship with the duty cycle $d_1$ of $S_1$. The wide $M_{\text{gain}}$ range satisfies different input voltage levels and prevents the rectifier from operating at extreme duty cycles ($d_1 < 0.1$ or $d_1 > 0.9$).
3) ZCT-ON: Inductor currents $i_{\text{Lk}A}$, $i_{\text{Lk}B}$ and $i_{\text{Lk}C}$ are in DCM. Switch $S_1$ acquires ZCT-ON soft-switching and reverse recovery losses of diodes $D_1$–$D_6$ are also removed.
4) Adoption of film capacitors: Film capacitors with lower leakage current and small value are employed instead of electrolytic capacitors, so that the power losses in dc-link capacitors are reduced. This helps to improve the system efficiency especially at low power. Besides, thanks to the symmetrical structure of the rectifier, the dc-link voltage ripples are weakened by the interleaved connected capacitors $C_a$, $C_b$, and $C_c$.
5) Inherent low THD: The THD of input source currents $i_{\text{in}A}$, $i_{\text{in}B}$, and $i_{\text{in}C}$ (PMSG output currents) is limited

However, additional distortions would be introduced into input currents by flyback cells, although these cells can provide the beneficial high voltage gain. This can be briefly explained that according to the relationship of $i_{\mathrm{Lk}A}$ ($i_{\mathrm{Lk}B}$, $i_{\mathrm{Lk}C}$), the secondary side flyback currents $i_{\mathrm{PA}}$ ($i_{\mathrm{PB}}$, $i_{\mathrm{PC}}$), the transformer magnetizing currents $i_{\mathrm{Lm}A}$ ($i_{\mathrm{Lm}B}$, $i_{\mathrm{Lm}C}$), and the transformer turns ratio *N* as (1). Taking phase A for instance, it infers that if $i_{\mathrm{PA}}$ is removed, then $i_{\mathrm{Lk}A}$ $(= i_{\mathrm{Lm}A})$ will have a linear relationship with the input voltage $v_{\mathrm{in}A}$. The envelope curve of $i_{\mathrm{Lk}A}$ will be an ideal sine wave and same with the TSB DCM rectifier. Thus $i_{\mathrm{in}A}$, filtered by $C_f$, turns out to be nearly sinusoidal except the potential crossover distortion of DCM [35]. However, when flyback cells operate, $i_{\mathrm{PA}}$ varies along with the control signal $d_1$, and the $N{\cdot}i_{\mathrm{PA}}$ component is introduced into $i_{\mathrm{Lk}A}$, which brings in additional distortions to the $i_{\mathrm{Lk}A}$ envelope curve and also enlarges the distortion of $i_{\mathrm{in}A}$. Consequently, the larger $i_{\mathrm{PA}}$ is the more distortion exists in $i_{\mathrm{in}A}$. Besides, since $i_{\mathrm{PA}}$ transmits power to $C_a$ in each switching cycle of $S_1$, the amplitude of $i_{\mathrm{PA}}$ has a positive correlation with $V_F$. Thus to reflect the distortions in $i_{\mathrm{in}A}$, define distortion factor $M_{\mathrm{FM}}$ as $M_{\mathrm{FM}} = V_F/V_M$, and the larger $V_F$ possesses in $V_{\mathrm{bus}}$, the more the flyback cells influence the rectifier and the larger the $i_{\mathrm{in}A}$ distortions are

$$i_{\mathrm{Lk}A} = i_{\mathrm{Lm}A} + N \cdot i_{\mathrm{PA}}. \tag{1}$$

The flyback cells can improve the voltage gain and bring in distortions simultaneously. To obtain high $M_{\mathrm{gain}}$ at weak power and low distortions at high power, a tradeoff is made in the design of rectifier parameters, in which $M_{\mathrm{FM}}$ should be restrained under 0.5 at high power. The design method and detailed analysis about the rectifier are presented in previous work [36].

### *B. Single-Phase Dual Buck Full-Bridge Inverter*

A single-phase dual buck full-bridge inverter [37] is adopted as presented in Fig. 2. Free of the bridge shoot through and the dead time problems, this inverter harvests enhanced reliability.

Considering the low average speed and large fluctuations of the SWF, it is unreasonable for the GT-SWGS to maintain $V_{\mathrm{bus}}$ constant at high level and to keep grid-connected continuously. Otherwise, the persistent conduction and switching losses of the inverter's power switches will lower down the overall efficiency. In the proposed system, the inverter is prohibited from absorbing main grid power to control $V_{\mathrm{bus}}$ constant. It does not maintain the all-time sustainable and uninterrupted grid-tie generation, which differs from other GT-SWGS [16]–[23]. This characteristic makes the proposed GT-SWGS more practical and more efficient for low-power condition.

In this system, under the condition that the battery capacity and the input wind power are located in the predefined range or the condition that the battery has been fully charged, the input power, which comes from rectifier or battery pack, will increase $V_{\mathrm{bus}}$ to reach the minimum dc-link voltage demand $V_{\mathrm{bus-required}}$ and the inverter will be activated. The inverter starts grid-tie generation with the assistance of the battery. Furthermore, in the former condition, the battery only provides the lowest feasible power to help the inverter maintain grid-connected, so that the amount of captured wind power, which is directly transferred to the grid, can be maximized and the wind power utilization rate is promoted. Moreover, when the inverter reaches its set power limitation $P_{\mathrm{inv-max}}$ for device protection, it will work as a constant power load and lose the ability to control $V_{\mathrm{bus}}$ temporarily. Instead, $V_{\mathrm{bus}}$ will be controlled by the storage branch. The control method of dc-link voltage is presented in Section IV.

TABLE I
CONTROL MODES OF THE BIDIRECTIONAL DC–DC CONVERTER

| Mode | $S_2$ | $S_3$ | $S_4$ | $S_5$ |
|---|---|---|---|---|
| boost charge | On | Off | Off | PWM |
| buck charge | PWM | On | Off | Off |
| boost discharge | Off | Off | PWM | On |

### *C. Bidirectional DC–DC Converter and the Battery Pack*

The storage branch, composed of the bidirectional dc–dc converter and the battery pack, acts as an assistance to reinforce the system performance of weak power connection, dc-link voltage stabilization, and excess power absorption.

To handle the changeful wind speeds, the storage branch should be flexible to control the charge and discharge states of the battery pack. Thereby, the bidirectional dc–dc converter, which can alter the equivalent circuit flexibly, is employed as shown in Fig. 2. It is made up of switches $S_2 - S_5$, inductor $L_{\mathrm{bat}}$, and capacitor $C_{\mathrm{bat}}$. By changing drive signals of the switches, corresponding power paths are built for battery charge or discharge: when $V_{\mathrm{bus}} < V_{\mathrm{bat}}$, the boost charge dc–dc converter leads the power flowing from dc-link to battery; when $V_{\mathrm{bus}} > V_{\mathrm{bat}}$, the power is from dc-link to battery in the buck charge mode and flows inversely in the boost discharge mode. Table I lists the mode control signals.

As a significant component, the battery pack must be selected carefully. In SA-SWGS [9], [14], battery packs with low open circuit voltage (OCV) and large capacity are often employed as the cost-efficient solution. The battery prefers large capacity because the fully charged battery can be used as a stable power source, i.e., conducting grid-tie generation or carrying a dc load, and large capacity means longer power-on time. Then with same capacity, lower OCV means less battery cells and lower cost, and the simple buck converter can be utilized also.

However, in this paper, battery pack with small capacity and increased OCV is demanded because both of the efficiency and cost issues of the charge and discharge operations should be concerned. In grid-tie generation mode, $V_{\mathrm{bus}}$ is larger than 380 V, so OCV should be high enough, otherwise the boost discharge circuit would be operated at the extremely large duty cycle. While for weak power collection, the very low dc-link voltage requires low OCV. Therefore, a middle OCV between 90 and 150 V is suitable. In terms of capacity, it is very hard for the SWGS to charge the large capacity battery in SWF, owing to the restrained wind power and more severe battery self-discharge. Accordingly, a small capacity battery pack is chosen because of the fast charge and slight battery self-discharge. The cost reduces also, which is a significant design objective for the SWGS.

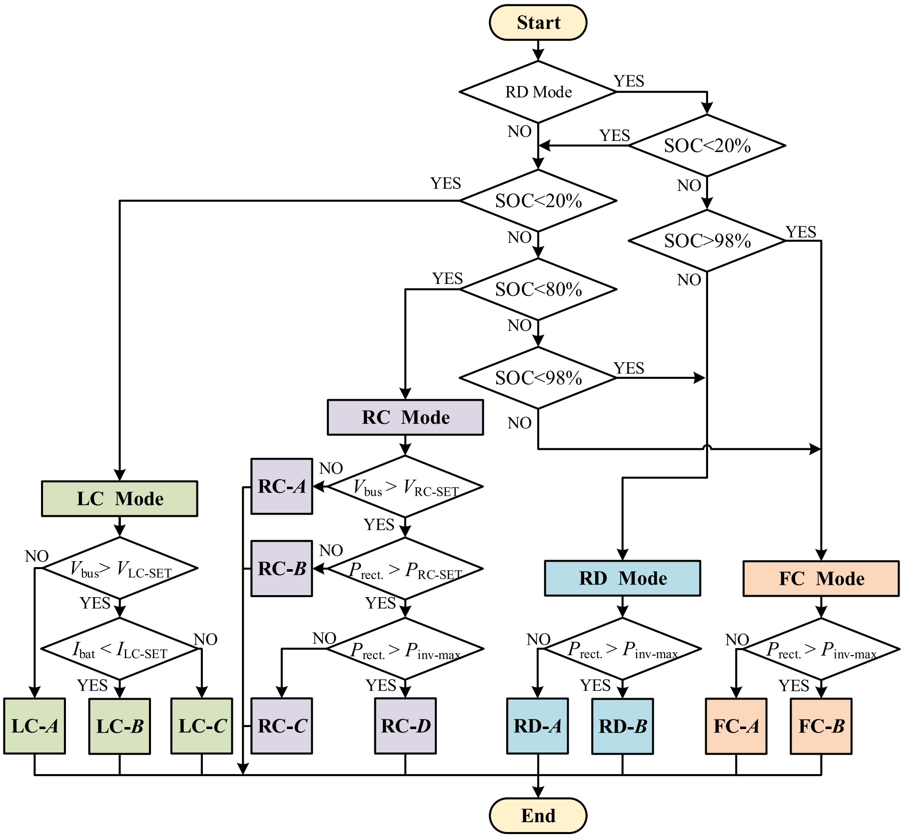

Fig. 3. Flowchart of the control strategy.

Despite the benefits of high power density, high efficiency, and long lifespan, the chosen Li-ion battery still suffers from the capacity fading problem [38]–[41]. For long-term operation, the crucial issue of battery fading prevention must be concerned. Although contradiction still exists on developing available methods to mitigate battery capacity fading, many researchers believe by preventing overcharge, overdischarge, and high *C*-rates, the capacity degradation can be weakened [38], [42]–[44]. Furthermore, studies [42]–[43] indicate the degradation rate remains low at charge rates $< 0.5\ C$, but will accelerate if high rate beyond 1 *C* is used. Literature [43] suggests the battery should be cycled with low-average SOC to limit the degradation rate. Thereby in this paper, the battery full-load charge rate is set at 0.5 *C* to avoid high *C*-rates, and the most frequent SOC range is set within 20–80% for overcharge and overdischarge prevention.

## III. CONTROL STRATEGY

The primary objective of the control strategy is to improve the performance of the proposed GT-SWGS concerning the limitations of practical wind field, especially at low-power condition (<300 W). Instead of acting as dc load as in many SA-SWGS, the controller manages the battery pack as an assistance to conduct grid-tie generation preferentially; meanwhile, it guarantees the battery lifespan extension as well:

1) in the frequent low-power condition (<30 W), the battery helps to collect weak input power, which always cannot be utilized by other GT-SWGS;
2) within middle power range (<260 W), the battery ensures the system is grid-connected, so that input wind power can be directly transferred to the grid for improved overall system efficiency; and
3) beyond middle power range (>260 W), for available HWS range expansion, the battery is commanded to absorb the surplus power.

To avoid over-charge, over-discharge and high *C*-rate current, the control strategy is divided into four main modes at first. Each mode corresponds to a certain battery SOC range as low-charge mode (*LC* mode, SOC <20%), ready-to-charge (*RC* mode, 20% ≤ SOC < 80%), ready-to-discharge mode (*RD* mode, 80% ≤ SOC < 98%), and full-charge mode (*FC* mode, 98% ≤ SOC). Then in order to deal with diverse wind speeds, each main mode is composed of several submodes. The flowchart of the control strategy is shown in Fig. 3.

Basically, the controller decides which main mode should be invoked by simply judging battery SOC. But if *RD* mode has been already chosen, the SWGS will stay in this main mode and keep discharging the battery until SOC falls below 20% or rises above 98%. This is because when SOC ≥ 80%, the battery is regarded to be fully charged and it is supposed to release most of the stored wind power persistently as a stable power supply for the grid-tie generation. Also through this method, the system normally works under *RC* and *RD* modes, and the *LC* and *FC* modes are not preferred so as to prevent overdischarge or overcharge, respectively. Besides, a variable step algorithm is transplanted to the proposed system for MPPT [45], [46].

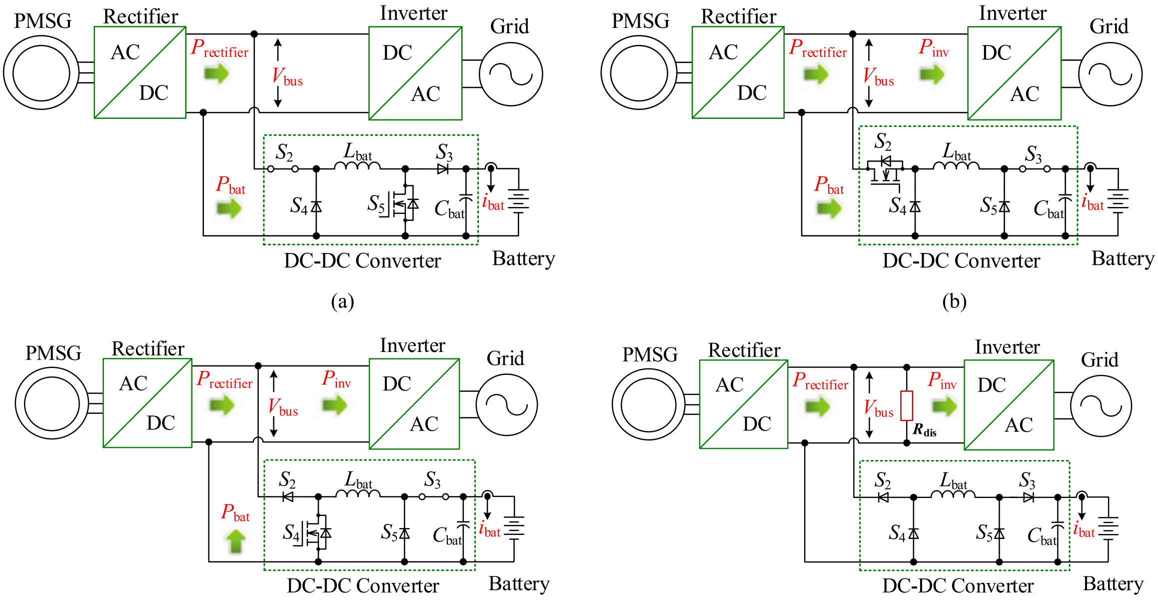

(a) (b)

(c) (d)

Fig. 4 Equivalent circuits of different working modes: (a) rectifier and boost charger, (b) rectifier, inverter, and boost charger, (c) rectifier, inverter, and boost discharger, and (d) rectifier and inverter.

### A. *Low-Charge Mode*

When SOC is below 20%, the system works in *LC* mode. Due to the low SOC, battery discharge may give rise to an accelerated capacity fading, and thus discharge is not allowed in this mode. Instead, the input power will be deposited in the battery preferentially. Usually, the grid-tie generation is not preferred also, unless the battery current $i_{\text{bat}}$ exceeds the full-load charge current $I_{\text{LC-SET}}$.

To accommodate variable wind speeds, *LC* mode is divided into three submodes, marked as *LC-A*, *LC-B*, and *LC-C*. When wind speed is low, $V_{\text{bus}}$ is restrained and cannot reach the dc-link voltage demand $V_{\text{bus-required}}$ even after boosted by the high step-up rectifier. The inverter is not activated and the input power is absorbed by the battery. For this weak power (<10 W), it is unnecessary for the boost charge dc–dc converter to implement any optimization algorithm. Instead, a simple fixed duty cycle control combining with the MPPT-based rectifier is suitable in *LC-A*.

Then, if $V_{\text{bus}}$ reaches the set voltage $V_{\text{LC-SET}}$, *LC-B* is adopted to charge the battery. $V_{\text{bus}}$ is stabilized at $V_{\text{LC-SET}}$, and any rise in input power only leads to the increase of the battery charge current $i_{\text{bat}}$. By this way, the control malfunction, caused by $V_{\text{bus}}$ fluctuations, to transform dc–dc converter's topology frequently is deterred. $V_{\text{LC-SET}}$ is set at about one-half of $V_{\text{bat}}$ so that the boost circuit could be operated within optimum duty cycle range. The power flow of *LC-A* and *LC-B* is presented in Fig. 4(a). The input power $P_{\text{in}}$ is stored in the battery $P_{\text{bat}}$ and is represented by the rectifier output power $P_{\text{rectifier}}$ ($P_{\text{in}} \approx P_{\text{rectifier}}$).

If $P_{\text{rectifier}}$ continues to rise and $i_{\text{bat}}$ reaches $I_{\text{LC-SET}}$, *LC-C* will dominate. To restrict high charge-rate, $i_{\text{bat}}$ is controlled by the buck charge converter beneath $I_{\text{LC-SET}}$, 0.5 *C* of battery capacity. The full-load charge power $P_{\text{char}}$ can be expressed as $P_{\text{char}} = I_{\text{LC-SET}} \times V_{\text{bat}}$. Meanwhile, since the input power is abundant, it is possible for the inverter to maintain the grid-tie generation. The surplus input power, represented by inverter power $P_{\text{inv}}$, is sent to the grid. The power relationship is shown as $P_{\text{rectifier}} = P_{\text{char}} + P_{\text{inv}}$ in Fig. 4(b).

The *LC* mode control logic is shown in Fig. 5(a), where a very simple but functional dead-zone controller is employed. The controller works at fixed switching frequency and has a dead-zone with upper border $V_{\text{high-border}}$ and lower border $V_{\text{low-border}}$. $V_{\text{bus}}$ is compared with $V_{\text{LC-SET}}$, and $i_{\text{bat}}$ is compared with $I_{\text{LC-SET}}$ at first to select the relevant submode. In *LC-A*, a fixed duty cycle control is implemented. In *LC-B*, if $V_{\text{bus}}$ exceeds $V_{\text{high-border}}$ ($= V_{\text{LC-SET}} + 1$ V here), the controller will increase the duty cycle $d_5$ of $S_5$ by $\Delta d$; else if $V_{\text{bus}}$ is smaller than $V_{\text{low-border}}$ ($= V_{\text{LC-SET}} - 1$ V here), $d_5$ will decrease by $\Delta d$. *LC-C* is invoked to fulfill the overcurrent protection. $V_{\text{bus}}$ is controlled by the activated inverter, and thus only a current dead-zone controller is adopted to control the buck charge converter. When the battery current exceeds the upper border of the zone, the duty cycle $d_2$ of $S_2$ will decrease by $\Delta d$; otherwise, a $\Delta d$ will be added to $d_2$. Finally, the PWM control signal, produced by the PWM generator, is sent to the dc–dc converter.

### B. *Ready-to-Charge Mode*

As the most frequently adopted mode, *RC* mode is chosen within SOC range 20–80%. This mode is multifunction and brings benefits including weak power collection, overall system efficiency enhancement and exploitable wind speed range expansion. Four RC sub-modes are marked as *RC-A*, *RC-B*, *RC-C*, and *RC-D*.

*RC-A* and *RC-B* are identical with *LC-A* and *LC-B*. Instead of dissipating in other GT-SWGS, the most frequent weak input

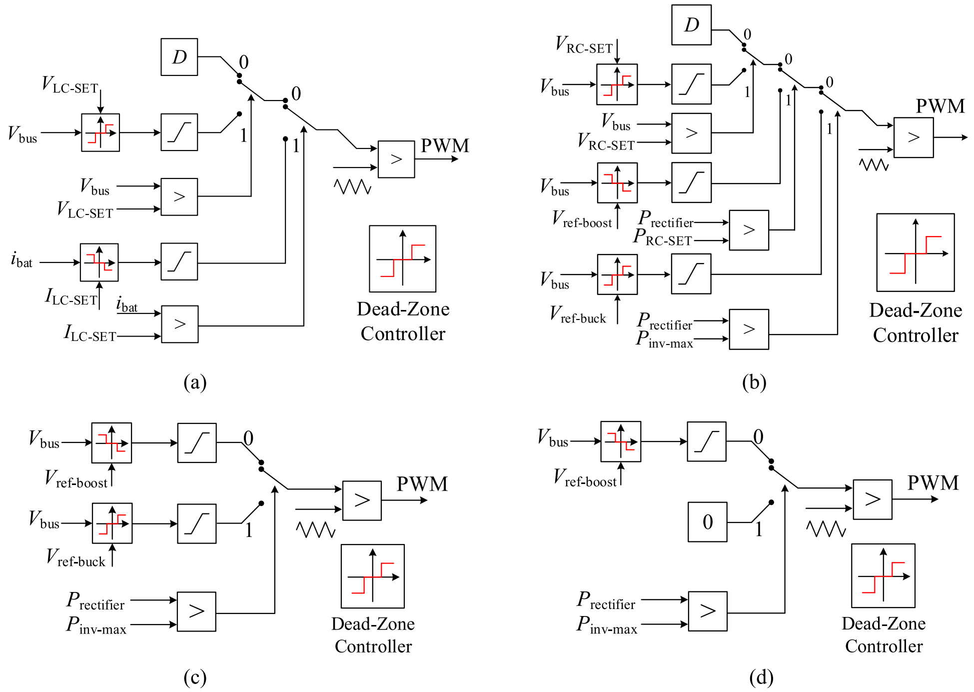

Fig. 5. Main mode control schematic charts: (a) *LC* mode, (b) *RC* mode, (c) *RD* mode, and (d) FC mode.

power ($P_{\text{rectifier}} < 30$ W), which cannot be delivered to the grid directly, is collected by the battery. The power utilization rate at LWS is thereby promoted.

When $P_{\text{rectifier}}$ reaches the set value $P_{\text{RC-SET}}$, the system enters *RC-C*. Rather than storing input power in the battery, the inverter is activated by the boost discharge dc–dc converter, and $P_{\text{rectifier}}$ is sent directly into the grid. Two main reasons account for this: 1) unlike *LC* mode, it is unnecessary to concern about the overdischarge issue; and 2) the direct power delivery from wind turbine output to grid eliminates the unwanted power dissipation during the transmission and storage procedures of the battery. Therefore, the overall system efficiency is promoted. Moreover, the main purpose of *RC-C* is to guarantee efficient wind power delivery, not to discharge battery capacity for stable power output. As a result, for battery capacity saving, the discharge power $P_{\text{bat}}$ should be limited at the lowest feasible dc–dc converter power $P_{\text{RC-low}}$, only to help the system to maintain grid connected. The power flow of *RC-C* can be described as $P_{\text{RC-low}} + P_{\text{rectifier}} = P_{\text{inv}}$ in Fig. 4(c).

If wind speed goes on increasing, the sum of the rising $P_{\text{rectifier}}$ and the constant $P_{\text{bat}}$ will approach the inverter power limitation $P_{\text{inv-max}}$ as $P_{\text{RC-low}} + P_{\text{rectifier}} = P_{\text{inv-max}}$. Then, along with the increase of $P_{\text{rectifier}}$, $P_{\text{bat}}$ reduces to keep the grid-tie generation power constant at $P_{\text{inv-max}}$ and to stabilize the dc-link voltage. *RC-C* ends when $P_{\text{rectifier}} = P_{\text{inv-max}}$.

Usually in other SWGS, HWS protection mechanisms as dummy loads or pitch control are employed to dissipate surplus power or to lower the wind power coefficient $C_p$ [10], [17], [21]. Anyway, energy losses are inevitable. However, the storage branch provides another possibility to shunt the surplus power. In *RC-D*, since $P_{\text{rectifier}} > P_{\text{inv-max}}$, the dc–dc converter turns to buck charge circuit. The redundant input power is absorbed and stored by the battery, while the inverter power is still kept constant at $P_{\text{inv-max}}$. Actually, the battery pack indeed extends the system's capacity so that the SWGS can be functional at higher wind speed. The power flow relationship of *RC-D* is given as $P_{\text{rectifier}} = P_{\text{bat}} + P_{\text{inv-max}}$ in Fig. 4(b).

In addition, in case of extreme HWS that $P_{\text{inv}} = P_{\text{inv-max}}$ and the battery charge current is 1 *C*, the wind turbine will be braked and the whole SWGS will be shut down for protection. The battery shut-down charge current is set at 1 *C* instead of the full-load charge current 0.5 *C* so that the exploitable HWS range can be broadened. Although the battery capacity fading rate is lower at 0.5 *C*, it will not balloon within 1 *C* [42], [43]. Besides, according to Fig. 1 and test results in real SWF, this case does not occur frequently and is often used as backup. In every main mode, there is a similar backup measure for extreme HWS protection, which will not be discussed in this paper.

Fig. 5(b) illustrates the control logic of *RC* mode. Three judgments between $V_{\text{bus}}$ and the set voltage $V_{\text{RC-SET}}$, $P_{\text{rectifier}}$ and $P_{\text{RC-SET}}$, $P_{\text{rectifier}}$ and $P_{\text{inv\_max}}$ are made to determine which submode is chosen. $V_{\text{ref-boost}}$ and $V_{\text{ref-buck}}$ are the given voltage references of the boost discharge circuit and the buck charge circuit, respectively. This part will be analyzed in Section IV.

### *C. Ready-to-Discharge Mode*

The *RD* mode is selected when SOC is between 80% and 98%. Its control objectives include stable power supply, overall system efficiency promotion, overcharge and high discharge rate prevention, and HWS range expansion. Only two submodes *RD-A* and *RD-B* compose this mode.

Since SOC is ≥80%, the battery, regarded as fully charged, tends to release most of its stored power. Consequently, if

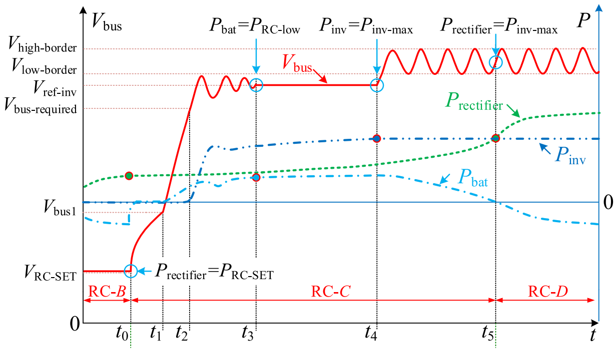

Fig. 6. DC-link voltage variation in *RC* main mode.

$P_{\text{rectifier}} < P_{\text{inv-max}}$, *RD-A* is invoked. The battery helps to establish the grid-tie generation and keeps on discharging until SOC drops lower than 20% and *LC* mode is invoked again as shown in Fig. 3. This control method brings benefits from four aspects:

1) Unlike the fluctuant wind source, the battery offers a stable power output and has less impacts on the grid.
2) Normally, SOC > 80% is achieved only when the wind power is abundant. Thus, after the discharge, the exhausted battery can be recharged quickly, and fast power delivery is realized. Besides, the input power is directly sent to the grid and high overall efficiency is also guaranteed.
3) Since battery capacity is released, the overcharge problem is avoided.
4) It ensures the battery is normally operated under 80% SOC, and leaves safety capacity margin in case of the extreme HWS. Consequently, this continuous discharge should persist as long as possible if the capacity is allowed.

Further for battery lifespan extension, high discharge rate should be avoided either. The maximum discharge current $I_{\text{dischar}}$ is set at 0.55 *C*, under which the fading rate is acceptable [42], [43]. In *RD-A*, the battery keeps discharging at $I_{\text{dischar}}$ continuously, the discharge power $P_{\text{dischar}}$ is calculated as $P_{\text{dischar}} = I_{\text{dischar}} \times V_{\text{bat}}$. Then, similar to *RC-C*, when $P_{\text{inv}} = P_{\text{inv-max}}$ is reached, the discharge power $P_{\text{bat}}$ decreases to keep power balance as $P_{\text{bat}} + P_{\text{rectifier}} = P_{\text{inv-max}}$ as shown in Fig. 4(c).

Like *RC-D*, when $P_{\text{rectifier}} > P_{\text{inv-max}}$, the system enters *RD-B*. The surplus power is stored into the battery for available HWS range expansion and $P_{\text{inv}}$ remains constant at $P_{\text{inv-max}}$. At this time, although the charge may force SOC exceed the optimum range of 20–80%, the capacity fading rate will not accelerate rapidly within SOC range of 80–98%. Besides, *RD-B* does not usually occur owing to the low average wind speed in SWF.

The control logic of *RD* mode is shown in Fig. 5(c). A deadzone controller is adopted and only one comparison between $P_{\text{rectifier}}$ and $P_{\text{inv-max}}$ is made to decide the PWM signal. The limit module in *RD-A* restricts the discharge power less than $P_{\text{dischar}}$.

### *D. Full-Charge Mode*

In the rare case of the continuous and sufficient wind power, SOC is beyond 98% and *FC* mode is chosen. Any charge fading, and thus only discharge is permitted. In *FC-A*, the battery discharges at $P_{\text{dischar}}$ as *RD-A*. If the wind speed goes on increasing and $P_{\text{rectifier}}$ is larger than $P_{\text{inv-max}}$ in *FC-B*, the protection method will be carried out. The dc–dc converter is shut down and a power-dissipative resistance $R_{\text{dis}}$ is connected to the dc-link for energy consumption. The power flow is presented in Fig. 4(d). Besides, Fig. 5(d) shows the *FC* control logic. The only difference from *RD* mode is that when $P_{\text{rectifier}} > P_{\text{inv\_max}}$, the dc–dc converter will be turned OFF for protection.

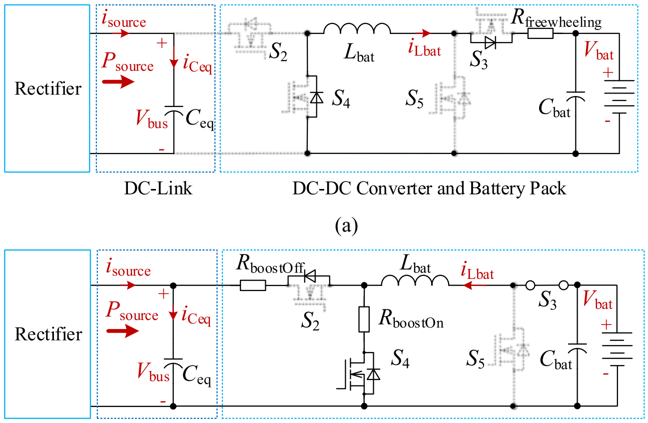

(a)

(b)

Fig. 7. Equivalent circuits of the dc–dc converter: (a) freewheeling period from $t_0$ to the moment $i_{L\text{bat}} = 0$ and (b) from $t_1$ to $t_2$.

## IV. DC-LINK VOLTAGE CONTROL

In this section, taking the most frequent *RC* mode for example. Suppose $P_{\text{rectifier}}$ varies as Fig. 6 shown, and the typical waveforms of dc-link voltage (left axis) and converter powers (right axis) are shown in Fig. 6. In *RC-C* and *RC-D*, the demand of inverter activation is satisfied and thus the inverter conducts grid connection. When operated as a separate converter, each of the dc–dc converter and the inverter has the ability to regulate the dc-link voltage $V_{\text{bus}}$ alone. However, when these two converters are combined in a single system, their coupling control effort may give rise to instability of the dc-link voltage. To avoid this, at the same time, only one converter will regulate $V_{\text{bus}}$, and the other one will be disabled to control $V_{\text{bus}}$ temporarily.

### *A. DC-Link Voltage Boosting Transition Analysis*

The system starts changing from *RC-B* to *RC-C* at $t_0$, and this part mainly explains the voltage variation process from $V_{\text{RC-SET}}$ to $V_{\text{bus-required}}$ during $t_0 - t_2$.

From $t_0$, the dc–dc converter should transform its topology from boost charge mode to boost discharge mode. However, since the current $i_{L\text{bat}}$ of $L_{\text{bat}}$ cannot change instantaneously, the battery should not discharge before $i_{L\text{bat}}$ decreases to zero. Switches $S_2 - S_5$ are turned OFF, and $i_{L\text{bat}}$ is absorbed by the battery and will fall to 0 before $t_1$. The equivalent circuit of the dc–dc converter is shown in Fig. 7(a). $V_{\text{bat}}$ is assumed as constant and the voltage variation of capacitor $C_{\text{bat}}$ is omitted. $C_{\text{eq}}$ is the equivalent capacitor of dc-link capacitors ($C_a$, $C_b$, $C_c$, By solving the KVL equation of the circuit in Fig. 7(a), the interval $t_{\text{freewheeling}}$ from $t_0$ to the moment when $i_{L\text{bat}} = 0$ can be expressed as (2), where $I_{L\text{bat}0}$ represents the initial current of $i_{L\text{bat}}$ at $t_0$.

Then, after $i_{L\text{bat}}$ drops to zero, the switches will remain off for an interval $t_{\text{suspend}}$ until $t_1$. Since the small $t_{\text{freewheeling}}$ (1.41 $\mu$s) is neglected, $t_{\text{suspend}}$ can be represented by the time span from $t_0$ to $t_1$. Also from Fig. 7(a), $P_{\text{source}}\ (= P_{\text{rectifier}} - P_{\text{inv}})$ represents the total equivalent power of the rectifier and the inverter, and since the inverter has not been activated yet ($P_{\text{inv}} = 0$), $P_{\text{source}}$ equals to $P_{\text{RC-SET}}$. It charges $C_{\text{eq}}$ to increase $V_{\text{bus}}$ and is assumed to be constant during $t_0$–$t_2$. $i_{\text{source}}$ is the relevant current of $P_{\text{source}}$. At $t_1$, the dc-link voltage $V_{\text{bus}}$ can be obtained as $V_{\text{bus1}}$

$$t_{\text{freewheeling}} = \frac{L_{\text{bat}}}{R_{\text{freewheeling}}} \ln\left[1 + \frac{I_{L\text{bat}0} \cdot R_{\text{freewheeling}}}{V_{\text{bat}}}\right] \tag{2}$$

$$V_{\text{bus1}} = \sqrt{\frac{2P_{RC\text{-SET}}}{C_{\text{eq}}} t_{\text{suspend}} + V_{RC\text{-SET}}^2}. \tag{3}$$

After $t_1$, the dc–dc converter is converted into boost discharge mode, and the equivalent circuit is shown in Fig. 7(b). $C_{\text{eq}}$ is charged by $P_{\text{source}}$ and the battery. $V_{\text{bus}}$ keeps on increasing until it reaches $V_{\text{bus-required}}$ (380 V) at $t_2$.

For the PWM controlled boost discharge converter, its inductor current $i_{L\text{bat}}$ can work under the continuous current mode (CCM) or the DCM. Thereby these two modes should be compared to decide which one is adopted during $t_1$–$t_2$. By solving KCL and KVL equations of the equivalent circuit in Fig. 7(b), $i_{L\text{bat}}$ and $V_{\text{bus}}$ can be calculated. $T_s = 50\ \mu$s is the fixed switching period. $R_{\text{boostOn}}$, $R_{\text{boostOff}}$ and $D_{\text{on}}\ (= d_4)$, $D_{\text{off}}$ represent equivalent resistances and duty cycles of the on and off states of $S_4$, respectively, $I_{\text{LN}}$ and $V_{\text{bus}N}$ are initial values of $i_{L\text{bat}}$ and $V_{\text{bus}}$ in the $N$th switching cycle of $S_4$. When $S_4$ turns ON in the $N$th cycle, (4) is achieved. $I_{L\text{Non}} = i_{L\text{bat}}(D_{\text{on}}T_s)$ and $V_{\text{busNon}} = V_{\text{bus}}(D_{\text{on}}T_s)$ are initial values when $S_4$ is off

$$\begin{cases} i_{L\text{bat}} = \left(I_{\text{LN}} - \dfrac{V_{\text{bat}}}{R_{\text{boostOn}}}\right) \cdot e^{-\frac{R_{\text{boostOn}}}{L_{\text{bat}}} t} + \dfrac{V_{\text{bat}}}{R_{\text{boostOn}}} \\ V_{\text{bus}} = \sqrt{\frac{2P_{RC\text{-SET}}}{C_{\text{eq}}} t + V_{\text{bus}N}^2} \end{cases}. \tag{4}$$

Then, when $S_4$ is off, $i_{L\text{bat}}$ and $V_{\text{bus}}$ are expressed as (5) and (6). $I_{L\text{Noff}} = i_{L\text{bat}}(D_{\text{off}}T_s)$ and $V_{\text{busNoff}} = V_{\text{bus}}(D_{\text{off}}T_s)$ are terminal values when $S_4$ is OFF in the $N$th cycle. Equations (4)–(6) are suitable for both of the CCM and the DCM

$$\begin{cases} i_{L\text{bat}} = C_{\text{eq}} e^{-\alpha_{\text{off}} t}[(-\alpha_{\text{off}} M_{\text{off1}} + \beta_{\text{off}} M_{\text{off2}}) \cdot \cos(\beta_{\text{off}} t) \\ \qquad - (\beta_{\text{off}} M_{\text{off1}} + \alpha_{\text{off}} M_{\text{off2}}) \cdot \sin(\beta_{\text{off}} t)] - \dfrac{P_{RC\text{-SET}}}{V_{\text{busNon}}} \\ V_{\text{bus}} = e^{-\alpha_{\text{off}} t}[M_{\text{off1}} \cdot \cos(\beta_{\text{off}} t) + M_{\text{off2}} \cdot \sin(\beta_{\text{off}} t)] \\ \qquad + V_{\text{bat}} + \dfrac{P_{RC\text{-SET}} R_{\text{boostOff}}}{V_{\text{busNon}}} \end{cases} \tag{5}$$

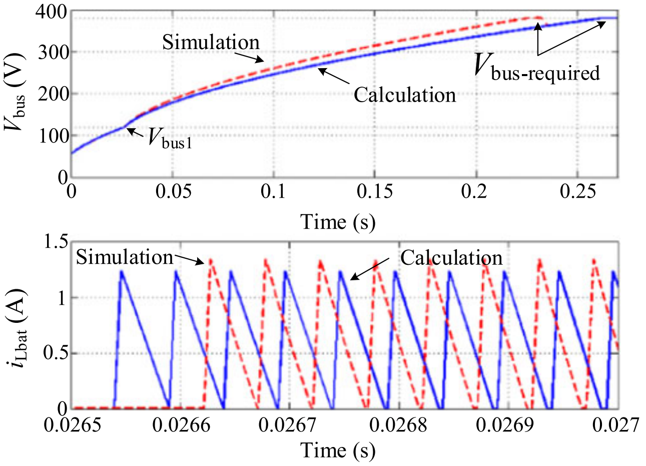

Fig. 8. Waveform comparison between simulation and iterative calculation during transition $t_0$–$t_2$.

$$\begin{cases} M_{\text{off1}} = V_{\text{busNon}} - V_{\text{bat}} - \dfrac{P_{RC\text{-SET}} R_{\text{boostOff}}}{V_{\text{busNon}}} \\ M_{\text{off2}} = \dfrac{ILNon + \dfrac{P_{RC\text{-SET}}}{V_{\text{busNon}}}}{C_{\text{eq}}\beta_{\text{off}}} \\ \qquad + \dfrac{\alpha_{\text{off}}\left(V_{\text{busNon}} - V_{\text{bat}} - \dfrac{P_{RC\text{-SET}} R_{\text{boostOff}}}{V_{\text{busNon}}}\right)}{\beta_{\text{off}}} \\ \alpha_{\text{off}} = \dfrac{R_{\text{boostOff}} C_{\text{eq}} + \dfrac{L_{\text{bat}} P_{RC\text{-SET}}}{V_{\text{busNon}}^2}}{2L_{\text{bat}} C_{\text{eq}}} \\ \beta_{\text{off}} = \dfrac{\sqrt{4L_{\text{bat}} C_{\text{eq}} - \left(R_{\text{boostOff}} C_{\text{eq}} + \dfrac{L_{\text{bat}} P_{RC\text{-SET}}}{V_{\text{busNon}}^2}\right)^2}}{2L_{\text{bat}} C_{\text{eq}}} \end{cases}. \tag{6}$$

In case of CCM, $I_{\text{LNoff}}$ and $V_{\text{busNoff}}$ also represent initial values $I_{\text{LN+1}}$ and $V_{\text{busN+1}}$ of the $N + 1$th cycle. While in DCM, there is an extra state exists before the $N$+1th cycle, in which $i_{\text{Lbat}}$ remains zero ($I_{\text{LN+1}} = 0$), $C_{\text{eq}}$ is still charged by $P_{\text{source}}$ and $V_{\text{bus}}$ keeps increasing. As a result, $V_{\text{busN+1}}$ of the DCM can be expressed as follows:

$$V_{\text{bus}N+1} = \sqrt{\frac{2P_{RC\text{-SET}}}{C_{\text{eq}}}(1 - D_{\text{on}} - D_{\text{off}})T_s + V_{\text{busNoff}}^2}. \tag{7}$$

Through iterative computation, $i_{L\text{bat}}$ and $V_{\text{bus}}$ in every cycle can be obtained. If the dc–dc converter works under CCM during $t_1 - t_2$, a large global current peak $I_{\text{Lpeak}}$ will exist in $i_{L\text{bat}}$. This is because in each of the first several switching cycles, the current increment $\Delta i_{L\text{bat}}\ (= I_{\text{LN+1}} - I_{\text{LN}} > 0)$ is positive value, and $I_{\text{Lpeak}}$, as the sum of $\Delta i_{L\text{bat}}$ in these switching cycles is large, i.e., when $D_{\text{on}} = 0.4$ and $V_{\text{bus1}} = 55$ V, $I_{L\text{peak}}$ is 25.75 A by iterative calculation and 25.67 A by simulation.

Therefore, to prevent large $I_{L\text{peak}}$, DCM operation is selected here. Moreover, according to (4)–(6), $V_{\text{bus1}}$ should be larger than $V_{\text{bat}}$, otherwise $i_{L\text{bat}}$ will be always under CCM in the first

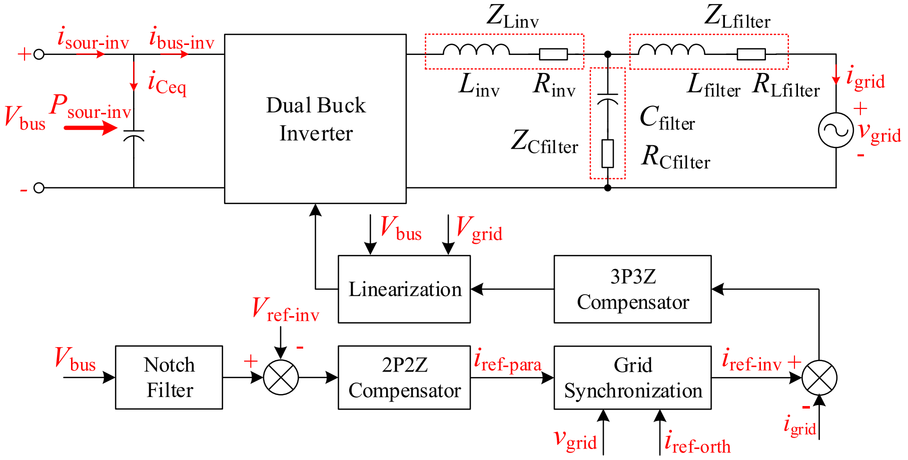

Fig. 9. Inverter control diagram.

several cycles. Finally, to simplify the control method in transition $t_1$–$t_2$, the dc–dc converter is operated under DCM with a fixed duty cycle $D_{\text{on}}$. The comparison between simulation and iterative calculation are shown in Fig. 8, where $i_{L\text{bat}}$ and $V_{\text{bus}}$ curves are drawn. It can be seen that when $V_{\text{bus1}} = 120$ V, both $i_{L\text{bat}}$ curves of the simulation and calculation work under DCM with a fixed $D_{\text{on}}$. The simulation $V_{\text{bus}}$ curve reaches $V_{\text{bus-required}}$ at $t_{\text{simu}} = t_2 - t_0 = 0.23$ s, while that of the calculation $V_{\text{bus}}$ curve is at $t_{\text{calc}} = 0.26$ s. However, in the actual experiment, instead of being the constant $P_{RC\text{-SET}}$, $P_{\text{source}}$ is often a fluctuant parameter, and thus the practical time span from $t_0$ to $t_2$ varies from 0.1 to 0.6 s.

### B. Inverter Control Method in RC-C

From $t_2$ to $t_4$, both of the boost discharge converter and the rectifier transfer power to the inverter. The front-end converters can provide sufficient power for the inverter and make sure $V_{\text{bus}}$ to reach the dc-link voltage demand $V_{\text{bus-required}}$, so the inverter operates and is able to control $V_{\text{bus}}$ through its dc-link voltage outer loop [47].

Before $V_{\text{bus}}$ is controlled by the inverter in steady state of $t_3 - t_4$, there is a transition period during $t_2 - t_3$. The inverter is activated at $t_2$. It absorbs power from dc-link and transfers this power to the ac grid. The battery pack discharges through the boost discharge dc–dc converter to provide power for the inverter. Assume $P_{\text{rectifier}}$ still remains $P_{\text{RC-SET}}$ during $t_2 - t_3$. The dc–dc converter increase $d_4$ by a fixed $\Delta d$ in every switching cycle of $S_4$ until $d_4$ reaches its duty cycle limitation $D_{\text{on-limit}}$. Then, with a constant $D_{\text{on-limit}}$, $P_{\text{bat}}$ is fixed at the lowest feasible dc–dc converter power $P_{\text{RC-low}}$, only to make sure the grid connection can be conducted with the sum of $P_{\text{RC-SET}}$ and $P_{\text{RC-low}}$. Since $i_{L\text{bat}}$ is still in DCM, $D_{\text{on-limit}} = 0.23$ is calculated through the power balance $P_{\text{bat}} = P_{\text{RC-low}}$ (neglecting the power loss) as follows:

$$P_{\text{bat}} = \frac{1}{T_s}\int_0^{T_s} V_{\text{bat}} i_{L\text{bat}} \cdot dt = P_{RC\text{-low}}. \tag{8}$$

Meanwhile, the inverter keeps the power balance between its input and output sides, and stabilizes $V_{\text{bus}}$. This transition ends at $t_3$. Then, in steady state of $t_3 - t_4$, the inverter continues to control $V_{\text{bus}}$, and the boost discharge converter can be regarded as a constant power source $P_{\text{RC-low}}$. The control diagram of the inverter is shown in Fig. 9. The voltage outer loop tracks the dc-link voltage reference $V_{\text{ref-inv}}$ and generates the current reference $i_{\text{ref-inv}}$ for the current inner loop. The current loop forces the grid-tie current $i_{\text{grid}}$ to track $i_{\text{ref-inv}}$. In the current loop, a three pole three zero compensator $G_{\text{ic}}(s)$ is employed to compensate the inherently unstable *LCL* filter of $Z_{\text{L}inv}$, $Z_{C\text{filter}}$, and $Z_{L\text{filter}}$, which is composed of the inverter inductor $L_{\text{inv1}}/L_{\text{inv2}}$ and a *LC* filter. The *LCL* plant is denoted as $G_{\text{p}}(s)$. Besides, a linearization module $H_{\text{line}}(s)$ is adopted to calculate the controlling duty cycle of the inverter by using the instantaneous sampled $V_{\text{bus}}$ and the grid voltage $v_{\text{grid}}$. Because the current loop gain at grid frequency is high (47 dB) and the crossover frequency (1.71 kHz) is much higher than the grid frequency; $v_{\text{grid}}$ and $V_{\text{bus}}$ are assumed as constant compared to the dynamics of $i_{\text{grid}}$. Detailed analysis is presented in literature [48]. Neglecting the current of capacitor $C_{\text{filter}}$, $G_{\text{p}}(s)$, and $G_{\text{ic}}(s)$ are presented as follows:

$$G_p(s) = \frac{Z_{C\text{filter}} + Z_{L\text{filter}}}{Z_{L\text{filter}} \cdot Z_{C\text{filter}} + (Z_{L\text{filter}} + Z_{C\text{filter}}) \cdot Z_{\text{L}inv}} \tag{9}$$

$$G_{ic}(z) = \frac{10.01z^3 - 26.39z^2 + 26.27z - 9.817}{z^3 - 2.297z^2 + 1.717z - 0.4204}. \tag{10}$$

Since $H_{\text{line}}(\text{s}) = 1$, the Bode diagram of the current loop is achieved by using similar method in [48]. The magnitude margin is 16.5 dB and the phase margin is 51.4°.

For voltage control loop as shown in Fig. 10, the error between $V_{\text{ref-inv}}$ and the filtered component $V_{\text{bus-fil}}$ of $V_{\text{bus}}$ is controlled by a 2P2Z compensator $G_{\text{vc}}(z)$ as (11). A grid synchronization module $H_{\text{syn}}(\text{s})$ is used to generate a parallel component $i_{\text{ref-para}}$ and an orthogonal component $i_{\text{ref-orth}}$ of $i_{\text{ref-inv}}$, in which $i_{\text{ref-para}}$ is in phase with $v_{\text{grid}}$ and $i_{\text{ref-orth}}$ is orthogonal to $v_{\text{grid}}$, and thus the controller can regulate reactive power of the inverter [49]. Then, through the current loop, $i_{\text{ref-inv}}$, consisting of $i_{\text{ref-para}}$ and $i_{\text{ref-orth}}$, is tracked by $i_{\text{grid}}$, which can be decomposed into $i_{\text{grid-para}}$ and $i_{\text{grid-orth}}$ too

$$G_{\text{vc}}(z) = \frac{0.0003276z \cdot (z - 0.9994)}{(z-1) \cdot (z - 0.9932)}. \tag{11}$$

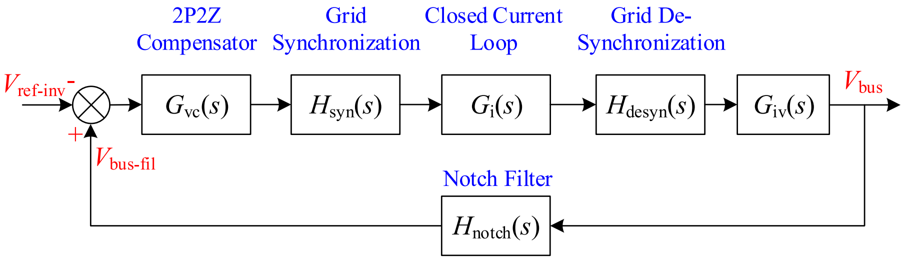

Fig. 10. Transfer function diagram of the voltage loop.

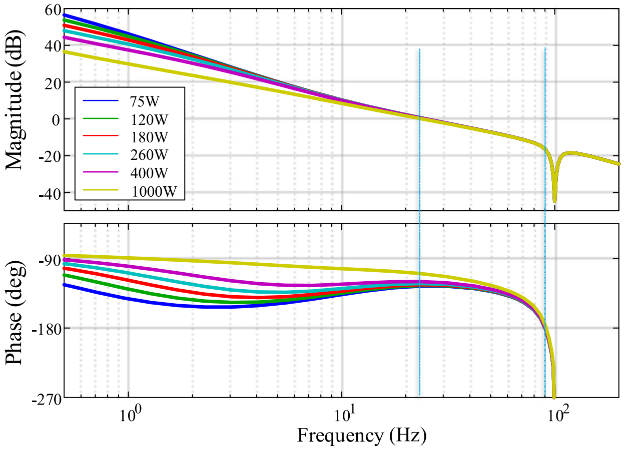

Fig. 11. Inverter voltage loop Bode diagram.

Also from Fig. 9, the inverter input current $i_{\text{bus-inv}}$ must meet the power balance equation as (12), in which $V_{\text{grid-amp}}$ and $I_{\text{grid-amp}}$ are the amplitudes of $v_{\text{grid}}$ and $i_{\text{grid}}$, $\omega_{\text{grid}}$ represents the grid angular frequency, and $\varphi$ is the phase difference between $v_{\text{grid}}$ and $i_{\text{grid}}$. Its dc component $I_{\text{bus-inv}}$ and double grid frequency ac component $i_{\text{bus-double}}$ can be obtained as (13), in which $v_{\text{grid-RMS}}$ and $V_{\text{bus-RMS}}$ are RMS values of $v_{\text{grid}}$ and $V_{\text{bus}}$. In this system, to pursue unity PF for $i_{\text{grid}}$, $\varphi$ is set at 0, namely $i_{\text{ref-orth}}$ is 0 and $i_{\text{grid-para}} = i_{\text{grid}}$

$$\begin{aligned} V_{\text{bus}} \cdot i_{\text{bus-inv}} &= v_{\text{grid}} \cdot i_{\text{grid}} \\ &= \frac{V_{\text{grid-amp}} I_{\text{grid-amp}}}{2} [\cos\varphi + \cos(2\omega_{\text{grid}} t - \varphi)] \end{aligned} \tag{12}$$

$$\begin{cases} I_{\text{bus-inv}} = \dfrac{v_{\text{grid-RMS}}}{\sqrt{2} V_{\text{bus}}} I_{\text{grid-amp}} \\ i_{\text{bus-double}} = \dfrac{V_{\text{grid-amp}} I_{\text{grid-amp}}}{2 V_{\text{bus}}} \cos(2\omega_{\text{grid}} t - \varphi) \end{cases}. \tag{13}$$

Through KCL equations of the dc-link side in Fig. 9 and linearization, $G_{\text{iv}}(s)$ is obtained as (14). $P_{\text{sour-inv}}$ is the equivalent power of $P_{\text{rectifier}}$ and $P_{\text{bat}}$, varying from $P_{\text{RC-low}}$ + $P_{\text{RC-SET}}$ (75 W) to $P_{\text{inv-max}}$ (260 W)

$$\begin{aligned} G_{\text{iv}}(s) &= \frac{V_{\text{bus}}(s)}{I_{\text{bus-inv}}(s)} \cdot \frac{I_{\text{bus-inv}}(s)}{I_{\text{grid}}(s)} \\ &= -\left(\frac{P_{\text{sour-inv}}}{V_{\text{bus}}^2} + C_{\text{eq}} s\right) \cdot \frac{v_{\text{grid-RMS}}}{\sqrt{2} V_{\text{bus-RMS}}}. \end{aligned} \tag{14}$$

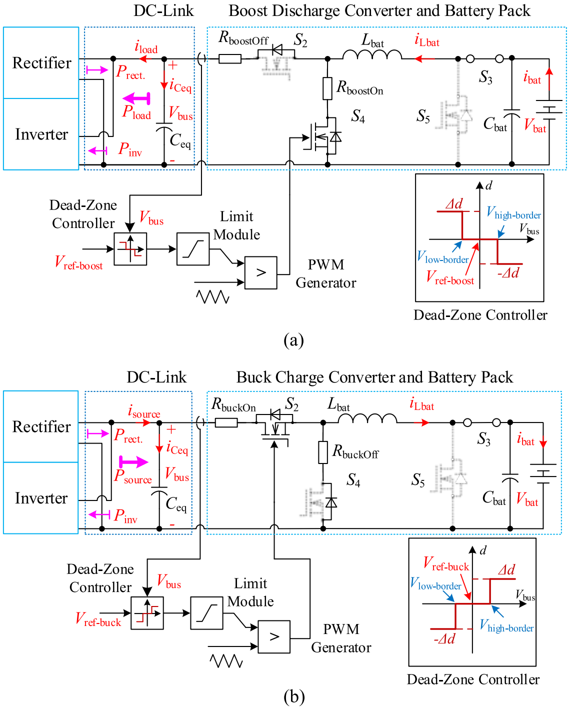

Fig. 12. DC–DC converter control diagram: (a) boost discharge mode and (b) buck charge mode.

To eliminate $i_{\text{bus-double}}$, a notch filter $H_{\text{notch}}(z)$ is adopted as follows:

$$H_{\text{notch}}(z) = \frac{z^2 - 2z + 0.9996}{z^2 - 1.9987z + 0.9988}. \tag{15}$$

Because the combined transfer function of $H_{\text{syn}}(\text{s})$ and the desynchronization module $H_{\text{desyn}}(\text{s})$ is 1, the voltage loop Bode diagram is obtained as Fig. 11 with the power varying from 75 to 260 W. The inverter presents good performance in the set power range, with amplitude margin from 16.4 to 16.5 dB and phase margin from 54.4° to 57.6°. The crossover frequency is nearly fixed at 24.8 Hz. For further high-power implementation, the Bode diagrams at 400–1000 W are also drawn in Fig. 11, where the amplitude margins are 16.6 and 17.1 dB and the phase margins are 60.0° and 70.3°.

### *C. DC–DC Converter Control Method in RC-C and RC-D*

When $P_{\text{inv}}$ reaches $P_{\text{inv-max}}$ at $t_4$, $i_{\text{ref-inv}}$ is restricted by the inverter's limit module. The inverter outputs a constant power and cannot control $V_{\text{bus}}$ after $t_4$. Instead, the boost discharge dc–dc converter regulates $V_{\text{bus}}$ as shown in Fig. 12(a).

A dead-zone control is used because of its benefits including independence from converter parameters, easy implementation, fast response, and suitability for low-power application [50]. In Fig. 12(a), when $V_{\rm bus}$ is smaller than the lower dead-zone border $V_{\rm low-border}$, the duty cycle will increase by one fixed step $\Delta d$ during one fixed switching cycle $T_s$, otherwise when $V_{\rm bus} > V_{\rm high-border}$, one $\Delta d$ will be subtracted. Thereby, $V_{\rm bus}$ is controlled within the dead-zone ($V_{\rm low-border}$, $V_{\rm high-border}$). The relationship of the $K$th duty cycle $d_{4({\rm K})}$ of $S_4$ and the $K+1$th $d_{4({\rm K}+1)}$ is presented as follows:

$$d_{4(K+1)} = \begin{cases} d_{4(K)} - \Delta d (V_{\rm bus} > V_{\text{high-border}}) \\ d_{4(K)} (V_{\text{high-border}} > V_{\rm bus} > V_{\text{low-border}}) \\ d_{4(K)} + \Delta d (V_{\rm bus} < V_{\text{low-border}}) \end{cases}. \qquad (16)$$

Similar as the analysis method as transition $t_1$–$t_2$, $V_{\rm bus}$ in each switching cycle of $S_4$ can be obtained by iterative computation. The iteration relation between the initial value $V_{\rm busK}$ in the $K$th cycle of $S_4$ and $V_{\rm busK+1}$ in the $K$+1th cycle is obtained as (17) and (18), where the definitions of parameters are similar to (4)–(7). $P_{\rm load}$ represents the ideal equivalent load power of $P_{\rm inv} - P_{\rm rectifier}$

$$\begin{cases} V_{\rm busKon} = \sqrt{V_{\rm busK}^2 - \dfrac{2P_{\rm load}}{C_{\rm eq}} D_{\rm on} T_s} \\ V_{\rm busKoff} = e^{-\alpha_{\rm boost} t}[M_{\rm boost1} \cdot \cos(\beta_{\rm boost} D_{\rm off} T_s) + \\ M_{\rm boost2} \cdot \sin(\beta_{\rm boost} D_{\rm off} T)] + V_{\rm bat} - \dfrac{P_{\rm load} R_{\rm boostOff}}{V_{\rm busKon}} \\ V_{{\rm bus}K+1} = \sqrt{V_{\rm busKoff}^2 - \dfrac{2P_{\rm load}}{C_{\rm eq}} (1 - D_{\rm on} - D_{\rm off}) T_s} \end{cases} \qquad (17)$$

$$\begin{cases} M_{\rm boost1} = V_{\rm busKon} + \dfrac{P_{\rm load} R_{\rm boostOff}}{V_{\rm busKon}} - V_{\rm bat} \\ M_{\rm boost2} = \dfrac{I_{\rm LKon} - \dfrac{P_{\rm load}}{V_{\rm busKon}}}{C_{\rm eq} \beta_{\rm boost}} \\ \qquad + \dfrac{\alpha_{\rm boost}\left(V_{\rm busKon} + \dfrac{P_{\rm load} R_{\rm boostOff}}{V_{\rm busKon}} - V_{\rm bat}\right)}{\beta_{\rm boost}} \\ \alpha_{\rm boost} = \dfrac{R_{\rm boostOff} C_{\rm eq} - \dfrac{P_{\rm load} L_{\rm bat}}{V_{\rm busKon}^2}}{2L_{\rm bat} C_{\rm eq}} \\ \beta_{\rm boost} = \dfrac{\sqrt{4L_{\rm bat} C_{\rm eq} - \left(R_{\rm boostOff} C_{\rm eq} - \dfrac{L_{\rm bat} P_{\rm load}}{V_{\rm busKon}^2}\right)^2}}{2L_{\rm bat} C_{\rm eq}} \end{cases}. \qquad (18)$$

Through (17) and (18), key parameters are obtained. Comprehensively considering the voltage ripple and the dynamic response, the performances with different dead-zone widths $H = (V_{\rm high-border} - V_{\rm low-border})/2$ and duty steps $\Delta d$ are compared. At last, $H$ of 1–3 V and $\Delta d$ of 0.005–0.015 are found to be suitable for this system by calculation, simulation, and experiment.

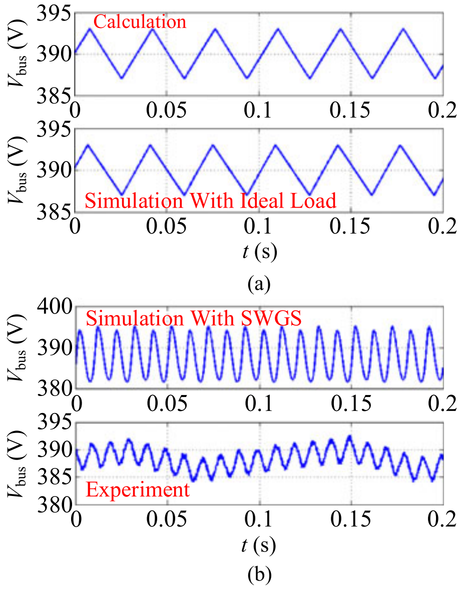

(a)

(b)

Fig. 13. Comparison of the boost converter control: (a) calculation and with ideal constant power load and (b) with SWGS and experiment.

The result is shown in Fig. 13, where $H = 3$ V, $\Delta d = 0.01$, $V_{\rm low-border} = 387$ V, and $V_{\rm high-border} = 393$ V are chosen. Fig. 13(a) shows that with ideal constant load $P_{\rm load}$, the calculation result is basically consistent with the simulation. The $V_{\rm bus}$ peak-to-peak value $v_{\rm bus-pp}$ is 6 V. However, in the practical SWGS, $P_{\rm load}$, varying in every switching cycle, is always not ideal. Consequently, the waveforms in Fig. 13(a) cannot match well with those of the simulation with SWGS ($v_{\rm bus-pp} = 11$ V) and the experiment ($v_{\rm bus-pp} = 5-10$ V) as presented in Fig. 13(b). Fortunately, in spite of the varying $P_{\rm load}$, the ripple in $V_{\rm bus}$ does not exceed 3% of 390 V, which is acceptable in the practical application.

When $P_{\rm rectifier}$ equals to $P_{\rm inv-max}$ at $t_5$, the dc–dc converter will change from boost discharge mode to buck charge mode in *RC-D*. The battery absorbs the surplus input power, and the buck charge converter controls $V_{\rm bus}$. The control diagram is shown in Fig. 12(b), and the analysis method is similar to that of boost discharge converter, except that the adjusting direction $\Delta d$ is reverse. The performance is tested in the Section V, where $H = 3$ V, $\Delta d = 0.01$, $V_{\rm low-border} = 387$ V, and $V_{\rm high-border} = 393$ V.

## V. EXPERIMENT RESULTS

To verify the performance of the proposed GT-SWGS, experiments based on a three-phase programmable ac voltage source and on a PMSG wind turbine are implemented, respectively. The prototypes of the converter and the wind turbine are presented in Fig. 14. The parameters of the GT-SWGS are listed in Table II. The battery pack consisting of 32 series-connected 3-Ah LiFePO$_4$ battery cells is adopted. The OCV varies within 96–116 V and the rated voltage is 106 V.

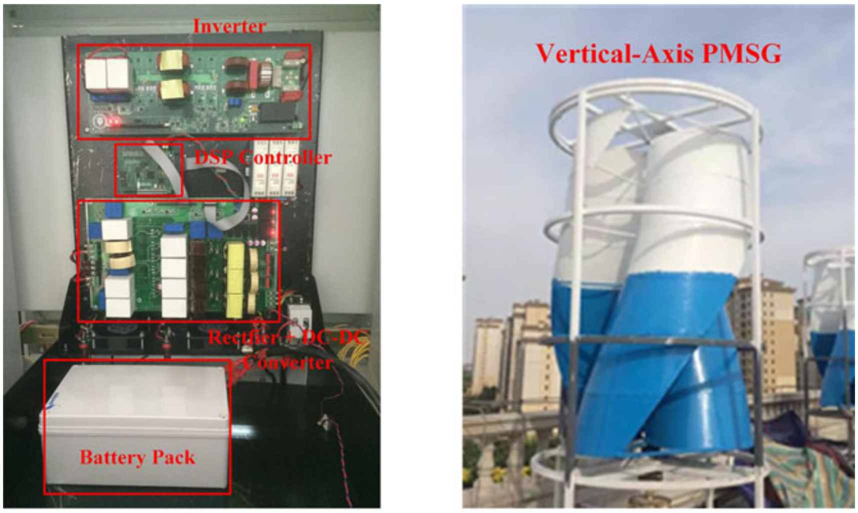

(a) (b)

Fig. 14. Experimental setups: (a) power electronic device and battery pack and (b) wind turbine.

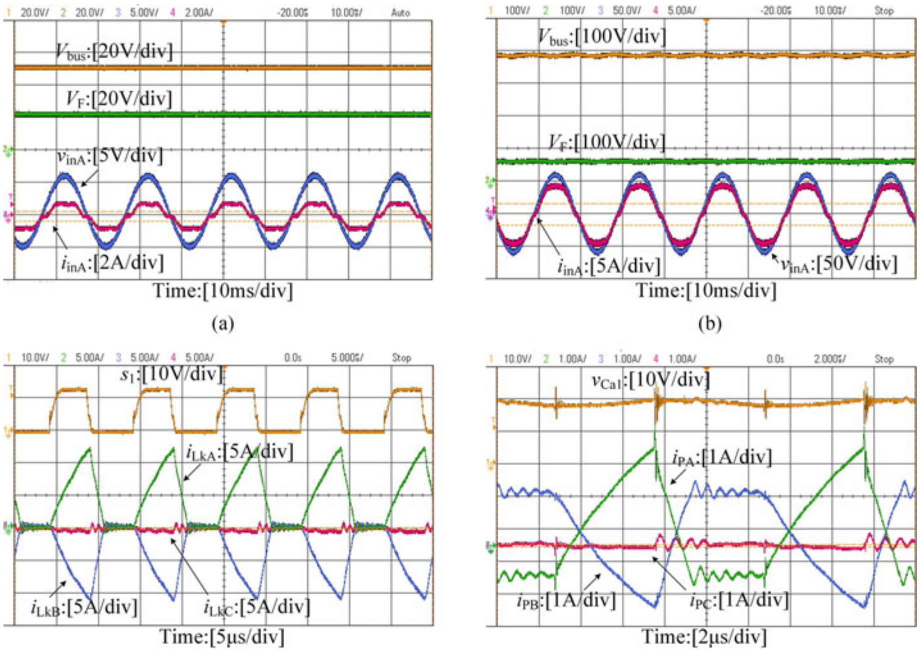

(a) (b)

(c) (d)

Fig. 15. Experimental waveforms of the rectifier: (a) voltage relationship at 6.8 W, (b) voltage relationship at 410 W, (c) $i_{{\rm Lk}A}$, $i_{{\rm Lk}B}$, and $i_{{\rm Lk}C}$ versus $s_1$ at 410 W, and (d) $i_{\rm PA}$, $i_{\rm PB}$, $i_{\rm PC}$, and $v_{\rm Ca1}$ at 410 W.

TABLE II
KEY PARAMETERS OF THE PROPOSED SYSTEM

| Parameters | Value |
|---|---|
| Equivalent leakage inductor $L_k$ | 18 $\mu$H |
| Transformer turn ratio $N$ | 3 |
| Flyback output capacitors $C_a$, $C_b$, $C_c$ | 40 $\mu$F |
| Inverter inductors $L_{\rm inv1}$, $L_{\rm inv2}$ | 1.5 mH |
| DC–DC converter inductor $L_{\rm bat}$ | 0.5 mH |
| Rectifier switching frequency | 100 kHz |
| DC–DC converter switching frequency | 20 kHz |
| Inverter switching frequency | 100 kHz |
| Rated grid voltage $v_{\rm grid-RMS}$ | 240-V RMS |
| PMSG | 1 kW, 200 r/min |

## *A. Rectifier Experiment*

Experiments are conducted on the proposed rectifier to validate its performance in the GT-SWGS. In Fig. 15(a), the rectifier is connected to the three-phase ac source at input side and to the battery pack at output side. The waveforms represent $V_{\rm bus}$, the flyback output voltage $V_F$, the input phase voltage $v_{{\rm in}A}$, and the input phase current $i_{{\rm in}A}$, respectively, at a small input power of 6.8 W, where $V_{\rm bus} = 50.7$ V, $V_F = 22$ V, $v_{\rm inA-RMS} = 3.85$ V, $i_{\rm inA-RMS} = 0.59$ A, and the duty cycle $d_1$ of $S_1$ is 0.7. The voltage gain $M_{\rm gain}$ is high at 13.2. The efficiency is 74%, while that in literature [9] is below 60% at 10 W. The distortion factor $M_{\rm FM}$ is calculated as 0.766 with a

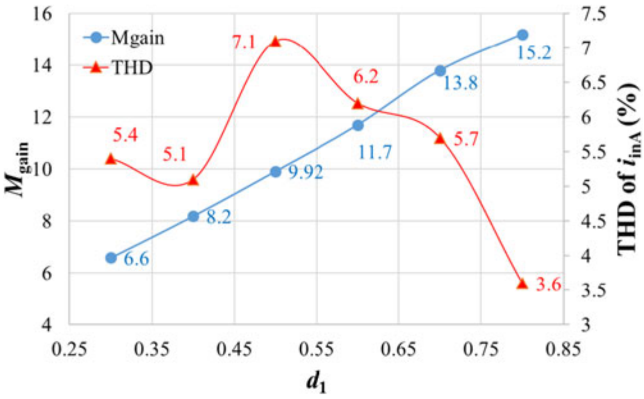

Fig. 16. Relationship of $M_{\text{gain}}$ and THD of $i_{\text{in}A}$ versus $d_1$.

12% THD in $i_{\text{in}A}$. Since the load is light, the influence of the $i_{\text{in}A}$ distortion can be neglected. Besides, $i_{\text{in}A}$ is in phase with $v_{\text{in}A}$ and high PF of 0.99 is obtained.

Fig. 15(b)–(d) are accomplished under the same condition, where the input power is raised to 410 W and the grid-tie generation is conducted. In Fig. 15(b), $V_{\text{bus}} = 385$ V, $V_F = 58.3$ V, $v_{\text{inA-RMS}} = 41.9$ V, $i_{\text{inA-RMS}} = 3.28$ A, and $d_1 = 0.45$ are obtained. $M_{\text{gain}}$ decreases to 9.2. The influence caused by flyback cells is weakened, and thus $M_{\text{FM}}$ diminishes to 0.18. The THD in $i_{\text{in}A}$ is restrained within 6.8%. The overall system efficiency is measured as 88.7% and the PF is 0.99.

Currents $i_{\text{Lk}A}$, $i_{\text{Lk}B}$, $i_{\text{Lk}C}$ and the PWM signal $s_1$ of $S_1$ are shown in Fig. 15(c), and because $v_{\text{in}C}$ is closed to zero at this instance, $i_{\text{Lk}C}$ closes to zero too. The DCM $i_{\text{Lk}A}$, $i_{\text{Lk}B}$, $i_{\text{Lk}C}$ remain zero before $S_1$ is turned ON, and thus $S_1$ achieves ZCT-ON. Since the influence of flyback cells is limited, $i_{\text{Lk}A}$, $i_{\text{Lk}B}$, and $i_{\text{Lk}C}$ contain weakened distortions and vary almost linearly.

Fig. 15(d) shows the transformer secondary side currents $i_{\text{PA}}$, $i_{\text{PB}}$, $i_{\text{PC}}$ and the flyback capacitor voltage $v_{\text{Ca1}}$ at the same instance with Fig. 15(c). Part of the input power flows from the transformer primary side to the secondary side. Operating as the power snubbers, the switched capacitors (as $C_{a1}$ and $C_{a2}$) store the primary side power and deliver it to capacitors $C_a$, $C_b$, and $C_c$ eventually. Consequently, taking phase A, for example, $i_{\text{PA}}$ increases at first and then decreases when $C_{a1}$ releases power in a single cycle. $v_{\text{Ca1}}$ varies along with this power transmission also.

In Fig. 16, relationship of $M_{\text{gain}}$ and THD of $i_{\text{in}A}$ versus $d_1$ are achieved by experiments at 400 W. When $d_1$ increases from 0.3 to 0.8, $M_{\text{gain}}$ varies nearly linearly along with $d_1$ in a wide range from 6.6 to 15.2, and the THD ranges from 3.6% to 7.1%.

The characteristics of the rectifier are concluded as: at low power, it provides high gain and ZCT-ON soft-switching so that the weak input power is stored in the battery with improved efficiency; with adequate power, it expresses reduced voltage gain, restricted THD, and relatively high efficiency (88–91%). The rectifier is also suitable for wide input voltage range and, thus, shows good competitiveness in SWGS.

## *B. Main Mode Experiments*

To test the four main control mods, PSIM simulations and experiments are conducted and presented in Figs. 17 and 18, respectively. In Fig. 18(a)–(d), the waveforms represent $V_{\text{bus}}$, $i_{\text{grid}}$, $i_{\text{bat}}$, and PWM drive signals $s_5$, $s_2$, $s_4$ of switches $S_5$, $S_2$, $S_4$, respectively. In Fig. 18(e)–(h), the RMS waveforms of $i_{\text{grid}}$ and the duty cycles $d_5$, $d_2$, $d_4$ are presented by processing experimental data (corresponding to Fig. 18(a)–(d), respectively) through MATLAB. The experiments are implemented in laboratory using the three-phase ac source as input, and the inverter is connected to the grid. Some explanations are made to help understand these waveforms:

1) instead of the dc–dc inductor current $i_{L\text{bat}}$, the battery current $i_{\text{bat}}$ is presented, which is more distinct to observe;
2) the +/− boundary of $i_{\text{bat}}$ is marked, and the battery discharges when $i_{\text{bat}} < 0$, otherwise the battery is charged; and
3) the increase and decrease of $i_{\text{bat}}$ reflect the amplitude variation, i.e., "$i_{\text{bat}}$ (<0) decreases" means the battery discharges and $i_{\text{bat}}$ moves toward zero line.

Fig. 18(a) shows the submode changeovers of *LC* mode. During 0–8 s, the system is in ***LC-A***. $d_5$ is fixed at about 0.1 as seen in Fig. 18(e). The weak input power is stored in the battery. $V_{\text{bus}}$ rises along with the increase of $P_{\text{rectifier}}$, but because $P_{\text{rectifier}}$ is small (<10 W), $i_{\text{bat}}$ stays almost at 0. The system enters ***LC-B*** at 8 s when $V_{\text{bus}}$ reaches $V_{\text{LC-SET}}$ (55 V). Then, $V_{\text{bus}}$ is stabilized at $V_{\text{LC-SET}}$ and the increase of $P_{\text{rectifier}}$ only leads to the rise of $i_{\text{bat}}$, which infers the battery is charged to raise SOC. $i_{\text{bat}}$ reaches $I_{\text{LC-SET}}$ (0.5 *C* 1.5-A RMS) at 26.5 s and the battery reaches its full-load charge power $P_{\text{char}}$ (160 W).

If $P_{\text{rectifier}}$ continues to rise, the system starts to activate the inverter. Before the grid-tie generation is established, there is a transition period, during which the dc–dc converter is shut down. $P_{\text{rectifier}}$ is transferred into $C_{\text{eq}}$ to boost $V_{\text{bus}}$. Then, after the inverter is activated, the dc–dc converter changes to buck charge mode and starts to control $i_{\text{bat}}$ toward $I_{\text{LC-SET}}$. Before $i_{\text{bat}}$ reaches $I_{\text{LC-SET}}$ again, $P_{\text{bat}}$ is smaller than $P_{\text{rectifier}}$. The inverter transmits the power $P_{\text{rectifier}} - P_{\text{bat}}$ to the grid, and there is a peak existing in $i_{\text{grid}}$ as shown in Fig. 18(e) from 26.5 to 28 s. This transition ends when $i_{\text{bat}} = I_{\text{LC-SET}}$, and the system is in ***LC-C***. The inverter delivers the surplus input power into the grid, so that $i_{\text{bat}}$ is fixed at $I_{\text{LC-SET}}$ regardless of the power fluctuations. This can be seen from $i_{\text{bat}}$ and $i_{\text{grid-RMS}}$ during 35–50 s in Fig. 18(a) and (e), where a 40-W fluctuation has no influence on $i_{\text{bat}}$.

In Fig. 17(a), simulation waveforms present similar results, and the relationship of the absolute values of $P_{\text{rectifier}}$, $P_{\text{inv}}$, and $P_{\text{bat}}$ is also shown. The transition between ***LC-B*** and ***LC-C*** is 0.2 s, which is much shorter than the experimental result. After the turn-OFF of the dc–dc converter, $i_{\text{bat}}$ gets to $I_{\text{LC-SET}}$ quickly at $t = 1.68$ s, and thus the peak in $i_{\text{grid}}$ is small (0.7-A RMS). This difference exists because unlike the PMSG, the three-phase ac voltage source cannot provide a constant power during the transition, and will have an unexpected instantaneous output drop, which makes the experimental transition time longer than the simulation. In the practical PMSG-based SWGS, this transition could be shorter according to the simulation result.

Fig. 18(b) presents the waveforms of RC mode. From 0 to 19.5 s, the battery is charged for weak power collection in ***RC-A***

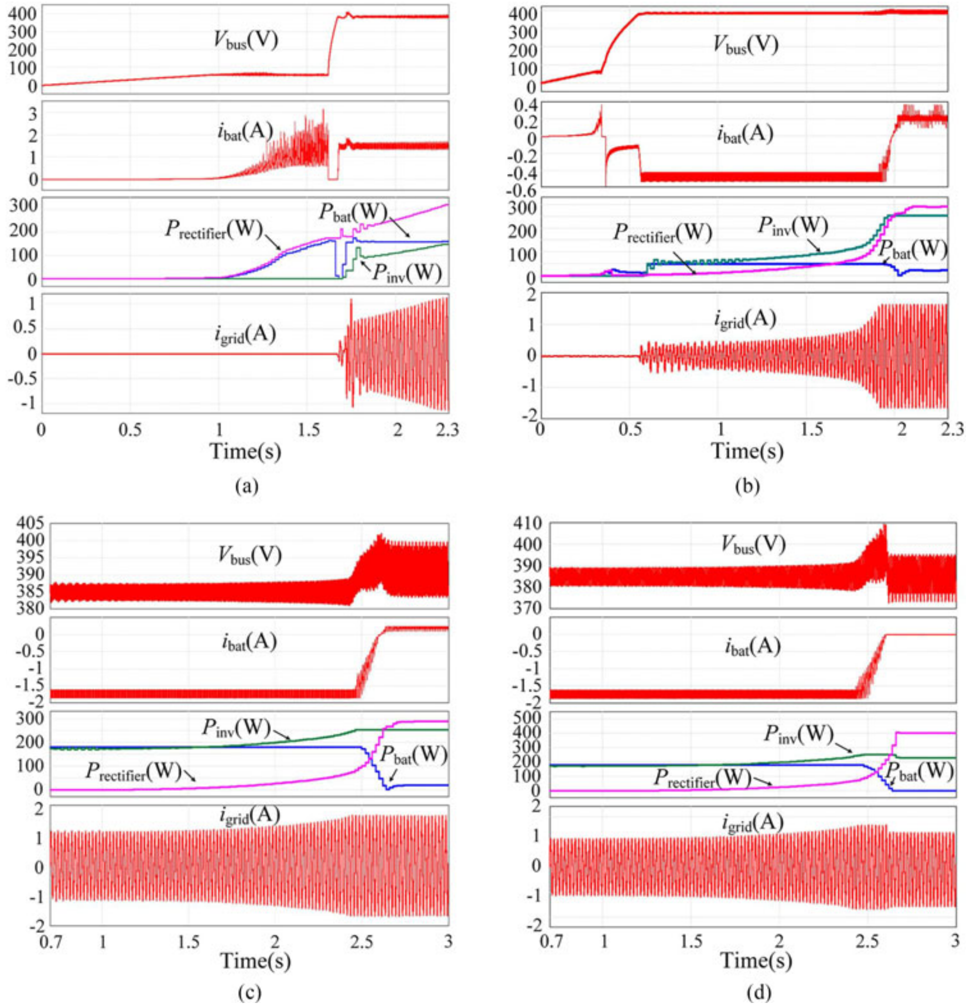

(a)

(b)

(c)

(d)

Fig. 17. Simulations of the main modes: (a) *LC* mode, (b) *RC* mode, (c) *RD* mode, and (d) *FC* mode.

and *RC-B*. The dc–dc converter is in the boost charge mode. $V_{\mathrm{bus}}$ raises from 0 to 55 V during 2–8 s, and then is fixed at $V_{\mathrm{RC-SET}}$ (55 V). $i_{\mathrm{bat}}$ rises from 8 to 19.5 s until the moment when $P_{\mathrm{rectifier}}$ reaches $P_{\mathrm{RC-SET}}$ (30 W). To improve the overall system efficiency, the system is operated in *RC-C* and $P_{\mathrm{rectifier}}$ is transferred directly to the grid. The transition between *RC-B* and *RC-C* is explained in Section IV. Measured in the experiment, the transition span $t_{\mathrm{exp}}$ $(= t_2 - t_0)$ is 0.4 s, which is longer than the calculation and simulation results. This is also caused by the unexpected power drop $\Delta P_{\mathrm{rectifier}}$ of the ac source. After this, for capacity saving, the boost discharge converter outputs at the set power limitation $P_{\mathrm{RC-low}}$ (45 W) as a constant power source and the grid-tie generation is implemented. The inverter controls $V_{\mathrm{bus}}$ at $V_{\mathrm{ref-inv}}$ (385 V) with voltage ripple less than ±4 V (1% of $V_{\mathrm{bus}}$). From Fig. 18(f), the grid-tie generation starts at $t = 20$ s. The inverter power is 72 W, and the battery discharge power is 42 W. This means that with the support of the battery pack, the grid-tie generation can be conducted with only a $P_{\mathrm{rectifier}} = 30\mathrm{W}$ input power. The grid-connection range is broadened and the overall system efficiency is guaranteed. Then, along with the rise of $P_{\mathrm{rectifier}}$, $i_{\mathrm{grid}}$ keeps increasing until $P_{\mathrm{inv}}$ meets $P_{\mathrm{inv-max}}$ (measured as 257.1 W) at 36.5 s. At this time, since $i_{\mathrm{grid}}$ will not increase any more, the inverter becomes a constant power load and cannot track $V_{\mathrm{ref-inv}}$ temporarily. Instead, the boost discharge converter controls $V_{\mathrm{bus}}$ through the dead-zone controller. $V_{\mathrm{bus}}$ rises to 390 V with a 1.8% fluctuation, and $i_{\mathrm{bat}}$ moves toward zero. This mode ends at $t = 39$ s when $P_{\mathrm{rectifier}} = P_{\mathrm{inv-max}}$. A transition period exists during 39–39.5 s for safety margin, in which the buck charge converter is forced to operate at the beginning of *RC-D* to absorb power additionally. $S_2$ works in advance in this transition and $i_{\mathrm{bat}}$, $i_{\mathrm{grid}}$ change suddenly. This margin avoids the possible power sampling deviation and makes sure $P_{\mathrm{rectifier}} \leq P_{inv-\mathrm{max}}$ in this transition so that the potential fluctuations of $V_{\mathrm{bus}}$ can be removed. The comparison experiments are conducted in *RD* mode and another *RC* mode (not presented), and the results show that without this safety margin, a fluctuation of ±15 V of $V_{\mathrm{bus}}$ will occur. After that, in *RD-D*, the dc–dc converter transfers to the buck charge circuit. $V_{\mathrm{bus}}$ is controlled by the buck converter at 390 V with small fluctuations (1.8%). For HWS range expansion, the battery absorbs the surplus input power and thus $i_{\mathrm{bat}}$ increases.

The relevant simulation is shown in Fig. 17(b). The system converts from *RC-B* to *RC-C* during the transition period from

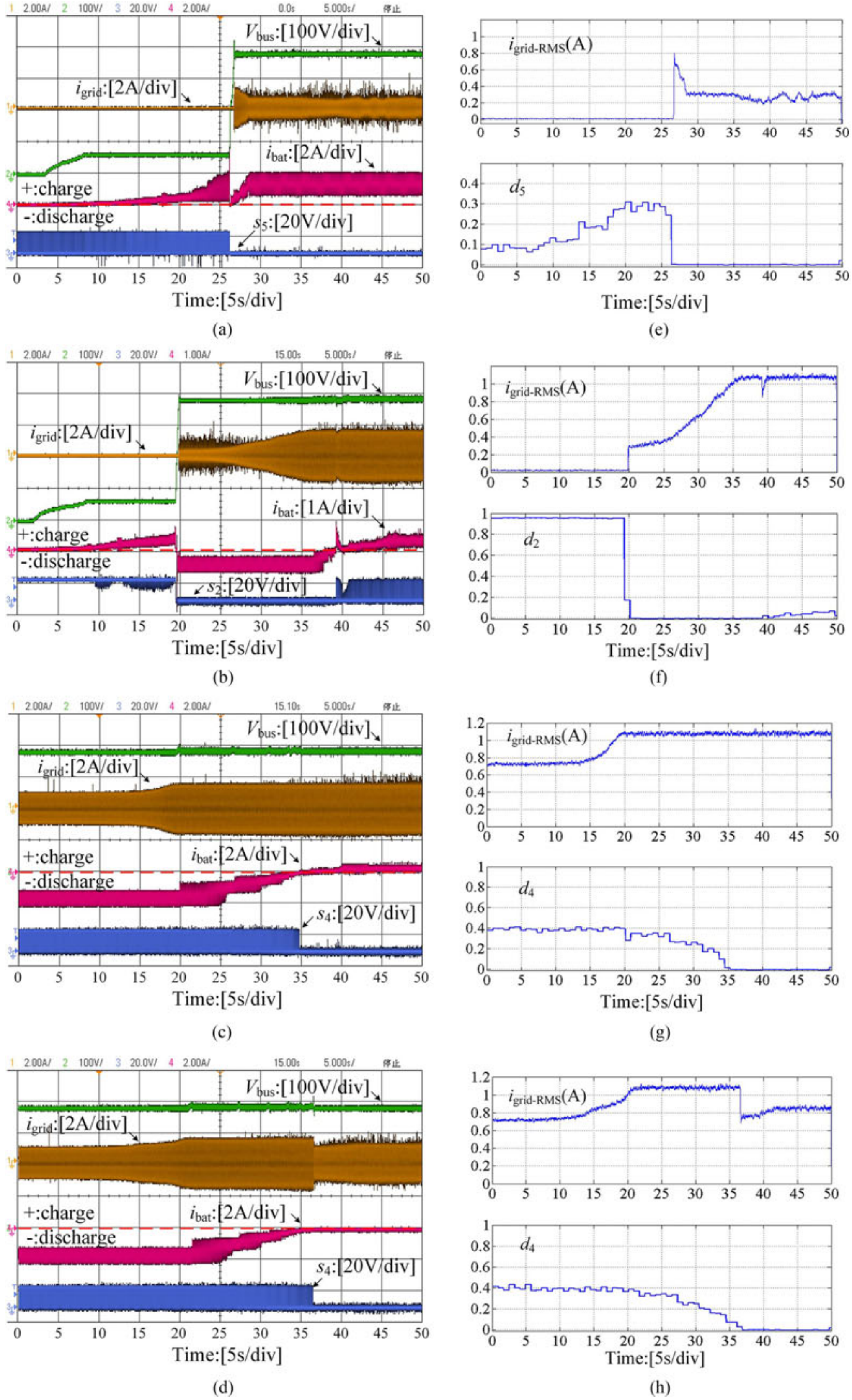

Fig. 18. Experimental waveforms of main modes (a) *LC* mode, (b) *RC* mode, (c) *RD* mode, (d) *FC* mode, (e) $i_{\mathrm{grid-RMS}}$ and $d_5$ of *LC* mode, (f) $i_{\mathrm{grid-RMS}}$ and $d_2$ of *RC* mode, (g) $i_{\mathrm{grid-RMS}}$ and $d_4$ of *RD* mode, and (h) $i_{\mathrm{grid-RMS}}$ and $d_4$ of *FC* mode.

0.33 to 0.56 s. The inverter stabilizes $V_{\rm bus}$ at $V_{\rm ref-inv}$ 385 ± 3 V in *RC-C*. And within 1.9–1.98 s and 1.98–2.3 s, $V_{\rm bus}$ is controlled at 390 V with fluctuations less than 3% by the boost converter and by the buck converter, respectively. $P_{\rm rectifier}$ promotes from 75 to 292 W within the interval 1.8–2.1 s, meanwhile the dc–dc converter keeps $V_{\rm bus}$ stable at 390 V with only a small fluctuation. This indicates the adopted dead-zone controller can provide acceptable dynamic response, which can be observed from the experimental waveforms as well.

In *RD* mode shown in Fig. 18(c), the battery discharge at $P_{\rm dischar}$ (178 W) for stable power supply. *RD-A* (0–35 s) is similar to *RC-C* except for the limit $D_{\rm on-limit}$ of $S_4$. In *RD-A*, $D_{\rm on-limit}$ is calculated as 0.42 and measured as 0.4 as shown in Fig. 18(g). After $P_{\rm inv} = P_{\rm inv-max}$ at 19 s, the inverter becomes a constant power load and the boost discharge converter controls $V_{\rm bus}$. Fig. 18(g) also shows that $d_4$ decreases to zero during 20–35 s, meanwhile in Fig. 18(c), $i_{\rm bat}$ gets to zero simultaneously. The system enters *RD-B* at $t = 35$ s. The battery takes in the surplus input power during 35–50 s as *RC-D*. The system enters *RD-B* at $t = 35$ s. For comparison, the safety margin between *RC-C* and *RC-D* is removed. A fluctuation of ±15 V occurs in $V_{\rm bus}$ as seen from 33.5 to 35.5 s. After this, the battery takes in surplus input power and guarantees $P_{\rm inv}$ constant at $P_{\rm inv-max}$ from 35 to 50 s.

The relevant simulation waveforms of *RD* mode are presented in Fig. 17(c). The battery outputs constant power at 175 W in *RD-A* (0.7–2.45 s), and $V_{\rm bus}$ is stabilized at 385 ± 3 V. During 2.45–2.6 s, $V_{\rm bus}$ is at 390 with fluctuation $<3\%$, and $i_{\rm bat}$ and $P_{\rm bat}$ decrease to zero gradually. After 2.6 s, $P_{\rm inv}$ is fixed at $P_{\rm inv-max}$ (259 W measured by simulation). The battery takes in the surplus power $P_{\rm rectifier} - P_{\rm inv-max}$, and $V_{\rm bus}$ is controlled at 390 with fluctuation less than 3%.

Fig. 18(d) indicates that *FC-A* is identical with *RD-A*. However, when $P_{\rm rectifier} = P_{\rm inv-max}$ and $i_{\rm bat} = 0$ at 37 s, since the battery charge is forbidden for overcharge prevention, an energy-dissipative resistance is connected to the dc-link for system protection. Thus, a sharp fall occurs in $i_{\rm grid}$ at $t = 37$ s. The simulation result of *FC* mode is presented in Fig. 17(d), where the dc–dc converter is shut down at $t = 2.6$ s and the surplus power $P_{\rm rectifier} - P_{\rm inv}$ is dissipated by the resistance.

### *C. DC-Link Voltage Control Experiment*

The experiments of the dc-link voltage control are presented in Figs. 19 and 20. In Fig. 19, waveforms of $V_{\rm bus}$, $v_{\rm grid}$, $i_{\rm grid}$ and the ac component $v_{\rm bus-ac}$ of $V_{\rm bus}$ are presented. The rectifier and the boost discharge converter transfer power to inverter. $V_{\rm grid-RMS}$ is 239 V and $P_{\rm inv}$ is 241 W. $V_{\rm bus}$ is controlled at 385 V with a small ripple $v_{\rm bus-ac}$ of ±4 V (1%) by the inverter. The PF and THD of $i_{\rm grid}$ are about 0.99 and 4.5%. The results show that inverter's controller has good performance.

The waveforms of $V_{\rm bus}$, the inductor current $i_{L\rm bat}$ of $L_{\rm bat}$, the battery current $i_{\rm bat}$, and $v_{\rm bus-AC}$ are shown in Fig. 20(a). At this time, the inverter is a constant power load, and $V_{\rm bus}$ is only controlled by the boost discharge dc–dc converter. $P_{\rm load}$ is 40 W and the dead-zone controller is set as $V_{\rm low-border} = 387$ V, $V_{\rm high-border} = 393$ V, and $\Delta d = 0.01$. $V_{\rm bus}$ is controlled at 389 V and fluctuation $v_{\rm bus-ac}$ never exceed ±4 V (1%). Owing to the fluctuant $v_{\rm bus-AC}$, the dead-zone controller has to keep on adjusting the controlling duty cycle. Thus, $i_{L\rm bat}$ and $i_{\rm bat}$ vary regularly along with $v_{\rm bus-AC}$. The partially enlarged waveforms of Fig. 20(a) are presented in Fig. 20(b). $i_{L\rm bat}$ is in DCM. However, owing to the parasite parameters, an oscillation occurs after $i_{L\rm bat}$ drops to zero. As the filtered component of $i_{L\rm bat}$, $i_{\rm bat}$ varies along with $i_{L\rm bat}$.

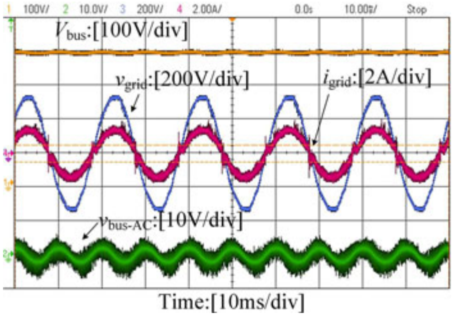

Fig. 19. Waveforms of dc-link voltage control by the inverter.

Similar waveforms of $V_{\rm bus}$, $i_{L\rm bat}$, $i_{\rm bat}$ and $v_{\rm bus-AC}$ are presented in Fig. 20(c). The surplus power $P_{\rm source}$ $(= P_{\rm rectifier} - P_{\rm inv})$ is 55 W, and $V_{\rm bus}$ is controlled at 388 V ± 4 V (1%) by the buck charge converter. In Fig. 20(d), the corresponding partially enlarged waveforms are also given. The oscillation caused by parasite parameters occurs after $i_{L\rm bat}$ drops to 0. $i_{L\rm bat}$ and $i_{\rm bat}$ are above zero, which means the battery takes in power from the dc-link. $i_{L\rm bat}$ is still in DCM and varies along with the PWM drive signal $s_2$.

From Fig. 20, the dead-zone controller shows reliable performance in controlling the dc-link voltage. $V_{\rm bus}$ is stabilized at around 389 V with fluctuation of ±4 V (1%). Then, from simulation results in Fig. 17(b), in which a 220 W variation of $P_{\rm rectifier}$ occurs within 0.3 s, the dead-zone controller keeps $V_{\rm bus}$ stable at 390 V with small distortions $<3\%$ and thus turns out good dynamic response. As a result, this simple dead-zone controller is proved to be functional and suitable for the proposed low-power GT-SWGS.

### *D. Available Power Range and Energy Production Analysis*

The experimental waveforms at low (12 W) and high (460 W) power are presented in Fig. 21. In Fig. 21(a), the input phase voltage $v_{{\rm in}A}$, the input phase current $i_{{\rm in}A}$, $V_{\rm bat}$, and $i_{\rm bat}$ are shown. $P_{\rm rectifier}$ is stored into the battery through the rectifier and the boost charge converter. $P_{\rm rectifier}$ is briefly calculated as 7.4V × 0.566 A × 3 = 12.56 W and $P_{\rm bat}$ is 9.63 W, and thus the efficiency is 77% at 12 W. This means the proposed GT-SWGS has the ability to collect weak input power at 12 W or even smaller. The system is able to store the weak power as long as the cut-in wind speed of the wind turbine is reached, and to conduct the grid-tie generation at $P_{\rm rectifier} = 30$ W in *RC* mode. Consequently, this system has a broadened low-power range and better performance at LWS compared with other GT-SWGS, in which this kind of weak power dissipates as heat.

In Fig. 21(b) $v_{{\rm in}A}$, $i_{{\rm in}A}$, $V_{\rm bat}$, and $i_{\rm bat}$ are also presented, where $P_{\rm rectifer} = 459.5$ W and $P_{\rm bat} = 152.3$ W. In Fig. 21(c),

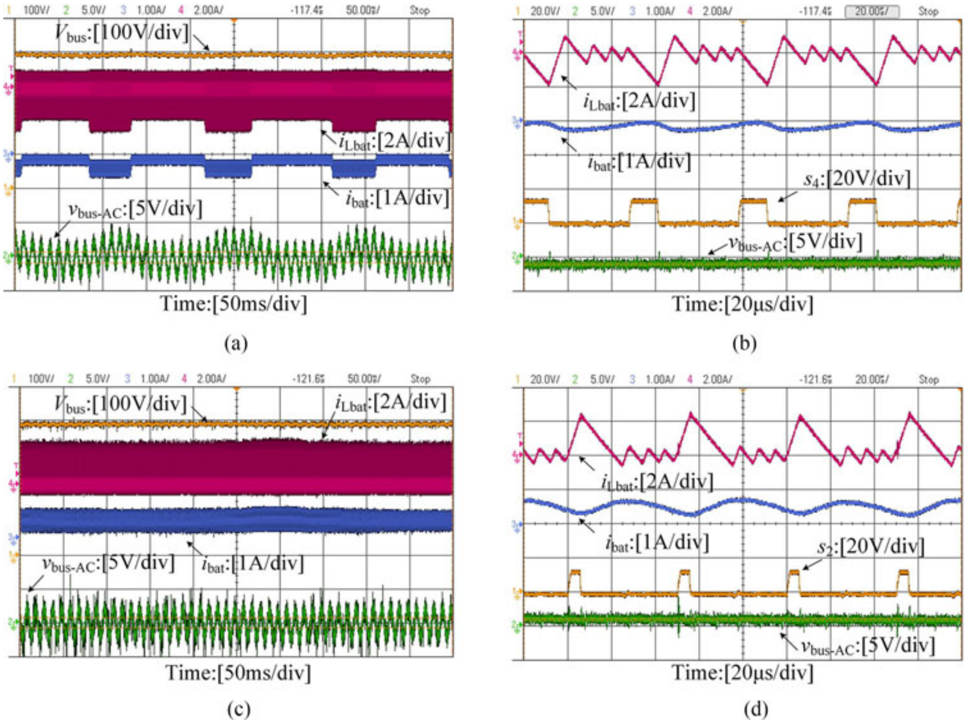

Fig. 20. Waveforms of dc-link voltage control by the dc–dc converter: (a) boost discharge circuit waveforms, (b) boost discharge circuit enlarged waveforms, (c) buck charge circuit waveforms, and (d) buck charge circuit enlarged waveforms.

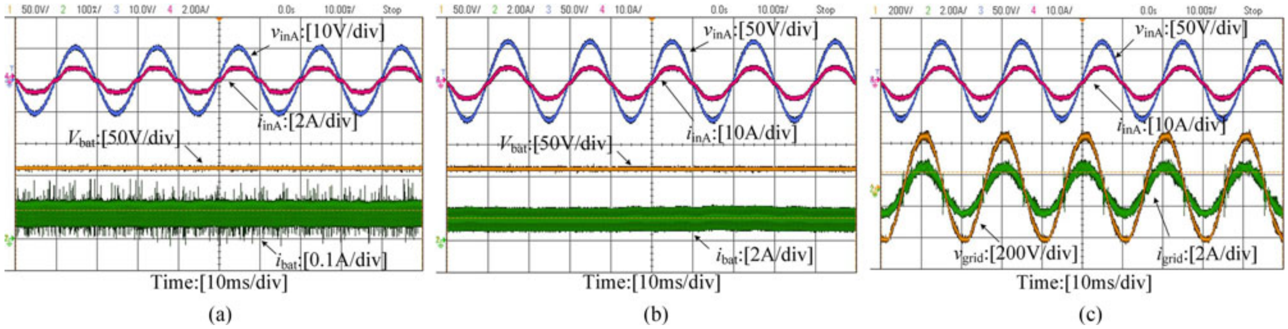

Fig. 21. Waveforms at 12 and 460 W: (a) input source and battery at 12 W, (b) and (c) input source and battery or inverter at 460 W.

$v_{\text{grid}}$ and $i_{\text{grid}}$ instead of $V_{\text{bat}}$ and $i_{\text{bat}}$ are shown. $V_{\text{grid}-\text{RMS}}$ is 239 V and $I_{\text{grid}-\text{RMS}}$ is 1.076 A. $P_{\text{inv}-\max}$ is calculated as 257.2 W and the overall system efficiency is obtained as $(P_{\text{bat}} + P_{\text{inv}-\max})/P_{\text{rectifier}} = 89\%$. Besides, since $i_{\text{in}A}$ is in phase with $v_{\text{in}A}$ and $i_{\text{grid}}$ is in phase with $v_{\text{grid}}$, high PFs (>0.99) in both of the input source side and the grid side are achieved.

The results indicate that the proposed SWGS can be operated within power range from 12 to 460 W with relatively high efficiency. By adopting the high step-up ZCT-ON rectifier and the battery pack, the LWS operation turns out to be better than other GT-SWGS, since it can collect weak wind power and conduct grid-tie generation at much lower input power. Considering the frequent low average power and fluctuations, the proposed SWGS is suitable for the SWF.

Moreover, the system configuration and control strategy of the proposed GT-SWGS can be transplanted to larger power level GT-SWGS. But limited by the experimental conditions, the maximum system power is accomplished at 460 W.

When the battery pack voltage and grid voltage are rated, and along with the change of input wind power or output battery power, the efficiencies of the converters are measured by YOKOGAWA WT3000 in the laboratory. Three curves are drawn in Fig. 22(a) including the rectifier-to-battery curve, the rectifier-to-inverter curve and the battery-to-inverter curve. These curves instead of the overall system efficiency curve are given for the reason that the submodes in each main mode are different and overall system efficiency is difficult to be drawn. From the figure, we know that the battery-to-inverter curve is the highest, but the combined efficiency of the sequential power transmission through the rectifier, the battery and the inverter is much lower than that of the rectifier-to-inverter curve. Consequently, the overall system efficiency is enhanced if the input power is

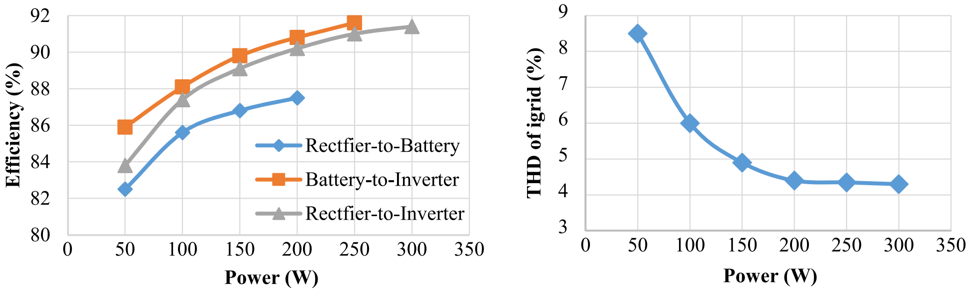

(a) (b)

Fig. 22. (a) Efficiency versus power and (b) THD of $i_{\mathrm{grid}}$ versus power.

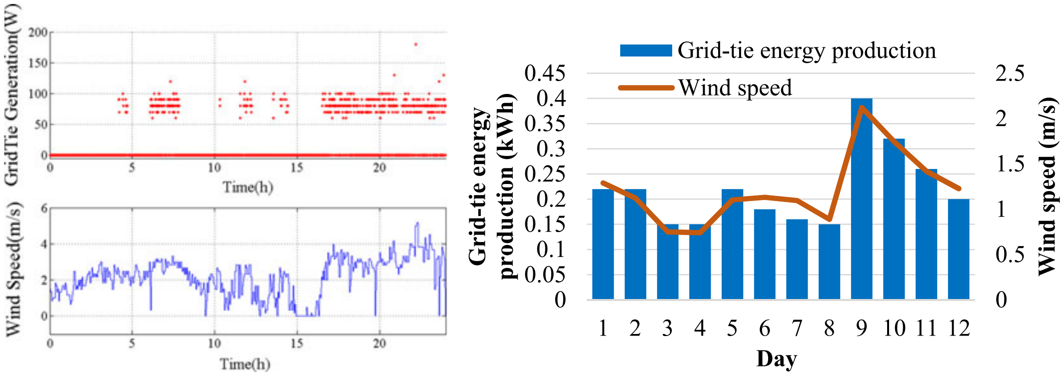

(a) (b)

Fig. 23. Performances of the proposed system in real SWF: (a) relationship between instantaneous grid-tie generation power and the wind speed of Day 9 and (b) grid-tie energy production in 12 days.

sent directly to the grid. The rectifier-to-inverter efficiency is beyond 90% when power level is above 200 W. In Fig. 22(b), the THD of $i_{\mathrm{grid}}$ versus power curve is also presented, where the THD is restrained under 4.6% at 200 W.

To verify the practicability, the proposed GT-SWGS has been tested in the real SWF for 12 days. The grid-tie generation data have been recorded and analyzed as shown in Fig. 23. Fig. 23(a) shows the relationship between the instantaneous grid-tie generation power and the wind speed of Day 9 as shown in Fig. 23(b). The 24-h data are sampled every 30 s and each of the wind speed points is the average value of five sampled points. When wind speed is above about 3 m/s, with the help of the battery, the GT-SWGS is able to conduct grid-tie generation. Along with the wind speed variation, the grid-tie power changes from 60 to 180 W. The maximum power is 180 W at about 5.3 m/s. When wind speed is below 3 m/s, the grid-connection stops and the weak wind power is stored into the battery. The daily grid-tie energy production is shown in Fig. 23(b). Each column represents a single day's energy production and the daily average wind speed is also given. The energy production has a positive correlation with wind speed. The total energy production is 2.63 kWh, while only 0.21 kWh is generated by a traditional GT-SWGS (diode bridge rectifier + boost converter + H-bridge inverter) during the same period. Both of the energy production data of the two systems are recorded by a local supervisory control and data acquisition system.

The adoption of the high step-up ZCT-ON rectifier and the storage branch leads to this difference in energy production. From Fig. 23(a), we know that even in the most production day, the wind speed is random and low. Without the rectifier and the battery, it is hard for the GT-SWGS to maintain a stable grid-tie generation. For most time, the weak input power dissipates, and thus the energy production is restricted in other GT-SWGS. Fortunately, through the proposed GT-SWGS, this weak power can be utilized and transferred to the grid eventually. Fig. 23 proves the adopted system has a good performance at LWS and is of high engineering practicality. However, since the wind speed in real wind field cannot be controlled, only the data of the most frequent *RC* mode are recorded, and other experiments are conducted in the laboratory.

## VI. CONCLUSION

A GT-SWGS is proposed in this paper. Based on improvements in both of the system configuration and the control strategy, the system shows high suitability for the SWF, where the average power is insufficient and the fluctuations are remarkable. In topology aspect, a novel high step-up ZCT-ON rectifier is applied and an additional storage branch is used. In controller aspect, relevant control strategy is adopted to strengthen the system's performance, especially for LWS and HWS conditions. At LWS, since high voltage gain and ZCT-ON is fulfilled by the rectifier, the controller commands the battery pack to absorb weak wind power with improved efficiency. The wind power utilization rate rises and good LWS operation is guaranteed. For middle wind speed range, the controller ensures the input power is transmitted directly to the grid for overall system efficiency promotion. In HWS condition, by adopting the dead-zone in the dc–dc converter, the surplus input power is stored in the battery, thus expanding the exploitable HWS range and the system power capacity. Besides, the battery lifespan extension is also taken into account by monitoring SOC. At last, through simulation and experiment, the feasibility is verified in the laboratory, and by testing in real SWF, the proposed GT-SWGS is proved to be effective, especially in LWS condition.

## REFERENCES

[1] (2015). World Wind Energy Report 2014. [Online]. Available: http://www.wwindea.org

[2] R. Doherty, H. Outhred, and M. O'Malley, "Establishing the role that wind generation may have in future generation portfolios," *IEEE Trans. Power Syst.*, vol. 21, no. 3, pp. 1415–1422, Aug. 2006.

[3] F. Blaabjerg, Z. Chen, and S. B. Kjaer, "Power electronics as efficient interface in dispersed power generation systems," *IEEE Trans. Power Electron.*, vol. 19, no. 5, pp. 1184–1194, Sep. 2004.

[4] Z. M. Dalala, Z. U. Zahid, W. Yu, Y. Cho, and J. S. Lai, "Design and analysis of an MPPT technique for small-scale wind energy conversion systems," *IEEE Trans. Energy Convers.*, vol. 28, no. 3, pp. 756–767, Sep. 2013.

[5] Z. M. Dalala, Z. U. Zahid, and J.-S. Lai, "New overall control strategy for small-scale WECS in MPPT and stall regions with mode transfer control," *IEEE Trans. Energy Convers.*, vol. 28, no. 4, pp. 1082–1092, Dec. 2013.

[6] A. M. Knight and G. E. Peters, "Simple wind energy controller for an expanded operating range," *IEEE Trans. Energy Convers.*, vol. 20, no. 2, pp. 459–466, Jun. 2005.

[7] R. Cisneros, F. M. David, and R. Ortega, "Passivity-based control of a grid-connected small-scale windmill with limited control authority," *IEEE J. Emerg. Select. Topics Power Electron.*, vol. 1, no. 4, pp. 247–259, Dec. 2013.

[8] (2015) Global climatic standard statistical data. [Online]. Available: data.cma.gov.cn

[9] E. Koutroulis and K. Kalaitzakis, "Design of a maximum power tracking system for wind-energy-conversion application," *IEEE Trans. Ind. Electron.*, vol. 53, no. 2, pp. 486–494, Apr. 2006.

[10] J. Chen, J. Chen, and C. Gong, "New overall power control strategy for variable-speed fixed-pitch wind turbines within the whole wind velocity range," *IEEE Trans. Ind. Electron.*, vol. 60, no. 7, pp. 2652–2660, Jul. 2013.

[11] J. W. Chen, J. Chen, and C. Y. Gong, "On optimizing the transient load of variable-speed wind energy conversion system during the MPP tracking process," *IEEE Trans. Ind. Electron.*, vol. 61, no. 9, pp. 4698–4706, Sep. 2014.

[12] A. S. Satpathy, N. K. Kishore, D. Kastha, and N. C. Sahoo, "Control scheme for a stand-alone wind energy conversion system," *IEEE Trans. Energy Convers.*, vol. 29, no. 2, pp. 418–425, Jun. 2014.

[13] J. Chen, J. Chen, and C. Gong, "Constant-bandwidth maximum power point tracking strategy for variable-speed wind turbines and its design details," *IEEE Trans. Ind. Electron.*, vol. 60, no. 11, pp. 5050–5058, Sep. 2013.

[14] K. Y. Lo, Y. M. Chen, and Y. R. Chang, "MPPT battery charger for stand-alone wind power system," *IEEE Trans. Power Electron.*, vol. 26, no. 6, pp. 1631–1638, Jun. 2011.

[15] S. Morimoto, H. Nakayama, H. Nakayama, and Y. Takeda, "Sensorless output maximization control for variable-speed wind generation system using IPMSG," *IEEE Trans. Ind. Appl.*, vol. 41, no. 1, pp.60–67, Jan./Feb. 2005.

[16] A. Mesemanolis, C. Mademlis, and I. Kioskeridis, "High-efficiency control for a wind energy conversion system with induction generator," *IEEE Trans. Energy Convers.*, vol. 27, no. 4, pp. 958–967, Jun. 2012.

[17] J. Chen and Y. Song, "Dynamic loads of variable-speed wind energy conversion system," *IEEE Trans. Ind. Electron.*, vol. 63, no. 1, pp. 178–188, Jan. 2016.

[18] L. Tan, Y. Li, C. Liu, and P. Wang, "An improved control strategy for the current source back-to-back converters," in *Proc. IEEE Int. Conf. Electr. Mach. Syst.*, Wuhan, China, 2008, pp. 1985–1989.

[19] R. Teodorescu and F. Blaabjerg, "Flexible control of small wind turbines with grid failure detection operating in stand-alone and grid-connected mode," *IEEE Trans. Power Electron.*, vol. 19, no. 5, pp. 1323–1332, Sep. 2004.

[20] Q. Wang and L. Chang, "An intelligent maximum power extraction algorithm for inverter-based variable speed wind turbine systems," *IEEE Trans. Power Electron.*, vol. 19, no. 5, pp. 1242–1249, Sep. 2004.

[21] H. Wang, C. Nayar, J. Su, and M. Ding, "Control and interfacing of a grid-connected small-scale wind turbine generator," *IEEE Trans. Energy Convers.*, vol. 26, no. 2, pp. 428–434, Jun. 2011.

[22] Y. Y. Xia, J. E. Fletcher, S. J. Finney, K. H. Ahmed, and B. W. Williams, "Torque ripple analysis and reduction for wind energy conversion systems using uncontrolled rectifier and boost converter," *IET Renewable Power Generation*, vol. 5, no. 5, pp. 377–386, 2011.

[23] S.-H. Song, S.-I. Kang, and N.-K. Hahm, "Implementation and control of grid connected ac–dc–ac power converter for variable speed wind energy conversion system," in *Proc. IEEE 18th Annu. Appl. Power Electron. Conf. Expo.*, 2003, pp. 154–158.

[24] Y. Zong, D. Kullmann, A. Thavlov, O. Gehrke, and H. W. Bindner, "Application of model predictive control for active load management in a distributed power system with high wind penetration," *IEEE Trans. Smart Grid.*, vol. 3, no. 2, pp. 1055–1062, Jun. 2012.

[25] M. Boobalan, S. Vijayalakshmi, and R. Brindha, "A fuzzy-PI based power control of wind energy conversion system using PMSG," in *Proc. Int. Conf. Energy Efficient Technol. Sustainability*, Nagercoil, India, 2013, pp. 577–583.

[26] A. Kusiak and Z. Zhang, "Adaptive control of wind turbine with data mining and swarm intelligence," *IEEE Trans. Sustain. Energy*, vol. 2, no. 1, pp. 28–36, Jan. 2011.

[27] W.-M. Lin and C.-M. Hong, "Intelligent approach to maximum power point tracking control strategy for variable-speed wind turbine generation system," *Energy*, vol. 35, no. 6, pp. 2440–2447, Jun. 2010.

[28] T. J. Liang and K. C. Tseng, "Analysis of integrated boost-flyback step-up converter," *Inst. Electron. Eng. Proc.: Elect. Power Appl.*, vol. 152, pp. 217–225, 2005.

[29] Y. Zhao, W. Li, Y. Deng, and X. He, "High step-up boost converter with passive lossless clamp circuit for non-isolated high step-up applications," *IET Power Electron*., vol. 4, no. 8, pp. 851–859, Sep. 2011.

[30] T. J. Liang, S. M. Chen, L. S. Yang, J. F. Chen, and A. Ioinovici, "A single switch boost-flyback DC–DC converter integrated with switched capacitor cell," in *Proc. 8th Int. Conf. Power Electron. ECCE Asia*, May/Jun. 2011, pp. 2782–2787.

[31] M. Prudente, L. L. Pfitscher, G. Emmendoerfer, E. F. Romaneli, and R. Gules, "Voltage multiplier cells applied to non-isolated DC–DC converters," *IEEE Trans. Power Electron.*, vol. 23, no. 2, pp. 871–887, Mar. 2008.

[32] Y. -P. Hsieh, J. -F. Chen, T. -J. Liang, and L. -S. Yang, "Novel high step-up DC–DC converter with coupled-inductor and switched-capacitor techniques," *IEEE Trans. Ind. Electron.*, vol. 59, no. 2, pp. 998–1007, Feb. 2012.

[33] Y. -P. Hsieh, J. -F. Chen, T. -J. Liang, and L. -S. Yang, "Novel high step-up DC–DC converter with coupled-inductor and switched-capacitor techniques for a sustainable energy system," *IEEE Trans. Power Electron.*, vol. 26, no. 12, pp. 3481–3490, Dec. 2011.

[34] K. Yao, X. Ruan, C. Zou, and Z. Ye, "Three-phase single-switch boost power factor correction converter with high input power factor," *IET Power Electron*., vol. 5, no. 7, pp. 1095–1103, Aug. 2012.

[35] K. Yao, X. Ruan, X. Mao, and Z. Ye, "Variable-duty-cycle control to achieve high input powerfactor for DCM boost PFC converter," *IEEE Trans. Ind. Electron.*, vol. 58, no. 5, pp. 1856–1865, May 2011.

[36] Y. F. Wang *et al.*, "High step-up 3-phase rectifier with fly-back cells and switched capacitors for small-scaled wind generation systems," *Energies*, vol. 8, no. 4, pp. 2742–2768, Apr. 2015.

[37] P. Sun, C. Liu, J. S. Lai, and C. L. Chen, "Cascade dual buck inverter with phase-shift control," *IEEE Trans. Power Electron.*, vol. 27, no. 4, pp. 2067–2077, Apr. 2012.

[38] M. A. Roscher, J. Assfalg, and O. S. Bohlen, "Detection of utilizable capacity deterioration in battery systems," *IEEE Trans. Veh. Technol.*, vol. 60, no. 1, pp. 98–103, Jan. 2011.

[39] N. Kakimoto and K. Goto, "Capacity-fading model of lithium-ion battery applicable to multicell storage systems," *IEEE Trans. Sustain. Energy*, vol. 7, no. 1, pp. 108–117, Jan. 2016.

[40] M. Dubarry and B. Y. Liaw, "Identify capacity fading mechanism in a commercial LiFePO4 cell," *J. Power Sources*, vol. 194, no. 1, pp. 541–549, 2009.

[41] L. Lam and P. Bauer, "Practical capacity fading model for Li-ion battery cells in electric vehicles," *IEEE Trans. Power Electron.*, vol. 28, no. 12, pp. 5910–5918, Dec. 2013.

[42] S. S. Choi and H. S. Lim, "Factors that affect cycle-life and possible degradation mechanisms of a Li-ion cell based on $LiCoO_2$," *J. Power Sources*, vol. 111, no. 1, pp. 130–136, 2002.

[43] K. Takei *et al.*, "Cycle life estimation of lithium secondary battery by extrapolation method and accelerated aging test," *J. Power Sources*, vol. 97, no. 7, pp. 697–701, 2001.

[44] H. Maleki and J. N. Howard, "Effects of overdischarge on performance and thermal stability of a Li-ion cell," *J. Power Sources*, vol. 160, no. 2, pp. 1395–1402, 2006.

[45] Q. Mei, M. Shan, L. Liu, and J. M. Guerrero, "A novel improved variable step-size incremental-resistance MPPT method for PV systems," *IEEE Trans. Ind. Electron.*, vol. 58, no. 6, pp. 2427–2434, Jun. 2011.

[46] H. Zhang, H. Ji, J. Ren, L. Shan, and Y. Gao, "Research on MPPT control and implementation method for photovoltaic generation system and its simulation," in *Proc. IEEE 6th Int. Power Electron. Motion Control Conf.*, Wuhan, China, 2009, pp. 2108–2112.

[47] T. F. Wu, C. L. Kuo, L. C. Lin, and Y. K. Chen, "DC-bus voltage regulation for a DC distribution system with a single-phase bidirectional inverter," *IEEE J. Emerg. Select. Topics Power Electron.*, vol. 4, no. 1, pp. 210–220, Mar. 2016.

[48] M. Bhardwaj, S. Choudhury, V Xue, and B. Akin, "Online LCL filter compensation using embedded FRA," in *Proc. IEEE 29th Annu. Appl. POWER Electron. Conf. Expo.*, 2014, pp. 3186–3191.

[49] X. Zong and P. W. Lehn, "Reactive power control of single phase grid tied voltage sourced inverters for residential PV application," in *Proc. 38th Annu. Conf. IEEE Ind. Electron. Soc.*, 2012, pp. 696–701.

[50] F. Zhang and J. Xu, "A novel PCCM boost PFC converter with fast dynamic response," *IEEE Trans. Ind. Electron.*, vol. 58, no. 9, pp. 4207–4216, Sep. 2011.

**Chengshan Wang** (SM'11) received the Ph.D. degree in electrical engineering from Tianjin University, Tianjin, China, in 1991.

From 1994 to 1996, he was a Senior Academic Visitor with Cornell University, Ithaca, NY, USA. From 2001 to 2002, he was a Visiting Professor with Carnegie Mellon University, Pittsburgh, PA, USA. He is currently a Professor in the School of Electrical Engineering and Automation, Tianjin University. He is the Director in the Key Laboratory of Smart Grid of Ministry of Education, Tianjin University. His current research interests include distribution system analysis and planning, distributed generation system and microgrid, and power system security analysis.

Dr. Wang is an Editor for the IEEE TRANSACTIONS ON SUSTAINABLE ENERGY. He is also an Editorial Board Member of *Applied Energy*, and *Journal of Modern Power Systems and Clean Energy*.

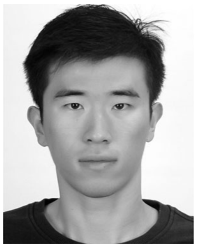

**Liang Yang** was born in Henan, China, in 1989. He received the B.S. degree in electrical engineering from Tianjin University, Tianjin, China, in 2013, where he is currently working toward the Ph.D. degree in electrical engineering.

His current research interests include small-scale wind generation and high-frequency planar magnetic-based dc–dc converter.

**Yifeng Wang** (S'09–M'12) was born in Hubei, China, in 1981. He received the B.S., M.S., and Ph.D. degrees in electrical engineering from Harbin Institute of Technology, Harbin, China, in 2005, 2007, and 2011, respectively.

Since 2011, he has been a Lecturer in the Department of Electrical and Electronics Engineering, Tianjin University. His interests include high-frequency and soft-switching power converters which are used for special power supply, EV charger, residential photovoltaic grid-connected generation system, distributed smart wind power generation system, and some other power conversion technology applications in hybrid AC/DC microgrid.

**Zhun Meng** was born in Jilin, China, in 1984. He received the B.S. and M.S. degrees from North China Electric Power University, Beijing, China, in 2007 and 2011, respectively. He is currently working toward the Ph.D. degree in electrical engineering from Tianjin University, Tianjin, China.

His current research interests include high-frequency inverter and electric vehicle charger.

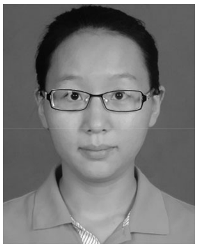

**Wei Li** was born in Hebei, China, in 1990. She received the B.S. degree in 2011 from Hebei University of Technology, Tianjin, China. She is currently working toward the Ph.D. degree in electrical engineering from Tianjin University, Tianjin, China.

Her current research interests include the modeling and control of power converters in distributed generations, and the stability and control of microgrids.

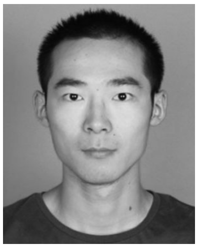

**Fuqiang Han** was born in Henan, China, in 1992. He received the B.S. degree in Tianjin Polytechnic University, Tianjin, China, in 2014. He is currently working toward the Ph.D. degree in electrical engineering from Tianjin University, Tianjin, China.

His current research interests include virtual synchronous generator.